nature communications

Article

https://doi.org/10.1038/s41467-024-52902-5

Aberrant cytoplasmic expression of UHRF1 restrains the MHC-I-mediated anti-tumor immune response

Received: 26 March 2024

Accepted: 24 September 2024

Published online: 03 October 2024

Check for updates

Lianmei Tan[1,8], Tao Yin[1,2,8], Handan Xiang[1,8], Liuyang Wang[3], Poorva Mudgal[4], Junying Chen[1], Yi Ding[1], Guoping Wang[2], Bryan Jian Wei Lim[2], Yuqi Huang[5], De Huang[1], Yaosi Liang[1], Peter B. Alexander[1], Kun Xiang[1], Ergang Wang[1], Chengsong Yan[1], Zhehao Ma[1], Minjia Tan[5], Qi-Jing Li[2,6,7] ✉ & Xiao-Fan Wang[1] ✉

Immunotherapy successfully complements traditional cancer treatment. However, primary and acquired resistance might limit efficacy. Reduced antigen presentation by MHC-I has been identified as potential resistance factor. Here we show that the epigenetic regulator ubiquitin-like with PHD and ring finger domains 1 (UHRF1), exhibits altered expression and aberrant cytosolic localization in cancerous tissues, where it promotes MHC-I ubiquitination and degradation. Cytoplasmic translocation of UHRF1 is induced by its phosphorylation on a specific serine in response to signals provided by factors present in the tumor microenvironment (TME), such as TGF-β, enabling UHRF1 to bind MHC-I. Downregulation of MHC-I results in suppression of the antigen presentation pathway to establish an immune hostile TME. UHRF1 inactivation by genetic deletion synergizes with immune checkpoint blockade (ICB) treatment and induces an anti-tumour memory response by evoking low-affinity T cells. Our study adds to the understanding of UHRF1 in cancer immune evasion and provides a potential target to synergize with immunotherapy and overcome immunotherapeutic resistance.

In recent years, immunotherapy has significantly improved the prognosis of patients with certain types of cancer[1,2]. The anti-cancer immunity process initiates with the priming and activation of immune cells by antigen-presentation cells. Upon recirculate into the tumor, the activated immune cells recognize cognate antigens presented on MHC molecules of tumor cells, leading to tumor cell destruction[3]. However, a majority of patients develop primary and acquired resistance to immunotherapy, with only a subgroup experiencing long-term benefits[4]. Resistance is a multifactorial process; as a part of cancer-immune co-evolution, cancer cells develop multiple intrinsic and extrinsic mechanisms to evade anti-cancer immunity[5]. For instance, impaired MHC-I antigen processing leads to acquired resistance to immune checkpoint blockade (ICB) treatment[6]. However, the complex molecular mechanisms whereby cancer cells restrain MHC-I remain to be further explored.

The tumor microenvironment (TME) plays a critical role in cancer development and progression[7]. Aberrant features frequently observed in the TME include hypoxia, abnormal vasculature, and altered

[1]Department of Pharmacology and Cancer Biology, Duke University School of Medicine, Durham, NC, USA. [2]Department of Immunology, Duke University School of Medicine, Durham, NC, USA. [3]Department of Molecular Genetics and Microbiology, Duke University School of Medicine, Durham, NC, USA. [4]TCRCure Biopharma, Durham, NC, USA. [5]State Key Laboratory of Drug Research, Shanghai Institute of Materia Medica, Chinese Academy of Sciences, Shanghai, China. [6]Institute of Molecular and Cell Biology (IMCB), Agency for Science, Technology and Research (A*STAR), Singapore, Singapore. [7]Singapore Immunology Network (SIgN), Agency for Science, Technology and Research (A*STAR), Singapore, Singapore. [8]These authors contributed equally: Lianmei Tan, Tao Yin, Handan Xiang. ✉e-mail: Li_QiJing@imcb.a-star.edu.sg; xiao.fan.wang@duke.edu

metabolism[8–10]. Notably, dynamic intercellular communications occur within the TME[7], resulting in biochemical cues that influence behaviors of both tumor and immune cells. Moreover, through the activities of immune-suppressive cells (such as regulatory T cells and myeloid-derived suppressor cells) and molecules (e.g., TGF-β and IL-10), the TME in solid tumors maintains an immune cold microenvironment[11], effectively shielding tumor cells from immune surveillance[12]. Through co-evolution with tumor cells, the TME can further inhibit anti-cancer immunity via hijacking mechanisms for selective advantage for tumor growth. For instance, tumor cells can reduce antigen presentation molecules through genetic or epigenetic regulation[13,14], leading to a suppressive TME. Conversely, a suppressive TME often reduces the production of interferons, potent stimulators of antigen presentation[15,16], further constraining anti-tumor immunity. Therapeutically facilitating the cold-to-hot transition in tumors could promote adequate T cell infiltration and mitigate immune suppression[11], thereby enhancing the efficacy of ICB therapy[17]. Consequently, developing strategies to overcome TME-induced immune suppression represents a promising avenue for enhancing the effectiveness of immunotherapy.

During cancer progression, tumor cells generally become more heterogeneous[18]. On the other hand, hosts develop a diverse tumor-reactive T cell repertoire comprised of TCRs with varying affinities[19,20]. In contrast to high-affinity T cells, those T cells targeting tumor-associated antigens (TAA) may express low-affinity TCRs as a result of thymic selection[19,21]. Functionally, high-affinity T cells against tumor-specific antigens (TSA) have a stronger effector response, whereas low-affinity T cells are more ready to form memory T cells as demonstrated in the context of infection[22,23]. However, MHC-I antigen presentation is often compromised in the TME[13,14], which may limit the formation of memory T cells critical for long term tumor control and recurrence. Therefore, restoring MHC-I expression on tumor cells could potentially elicit CD8+ T cell responses to endogenous low-affinity TAAs derived from poorly immunogenic tumors, thereby overcoming immunosuppression to achieve durable immunotherapy[23].

Here, we found that the epigenetic regulator UHRF1 is involved in cancer immune evasion by downregulating MHC-I expression. This process is enabled by UHRF1's aberrant cytosolic localization, triggered by phosphorylation in response to factors in the TME. Furthermore, UHRF1 inactivation synergizes with ICB and induces anti-tumor memory responses. These findings suggest that cytoplasmic UHRF1 could be a potential therapeutic target to enhance immunotherapy efficacy and address resistance in cancer treatment.

Results

UHRF1 is overexpressed in NSCLC and promotes tumor growth in syngeneic mouse models

Alterations of epigenetic marks have been observed in multiple physiological and pathological conditions, including autoimmune disorders, aging, and cancer[24,25]. UHRF1, a key epigenetic regulator, is well-documented to coordinate DNA methylation and histone modifications in the nucleus[26]. The PHD and SRA domains are critical for UHRF1 to maintain aberrant DNA methylation in colorectal cancer (CRC) cells[27]. Analysis of the TCGA database by TIMER 2.0[28–30] revealed that *UHRF1* mRNA is markedly upregulated in multiple cancer types, including lung adenocarcinoma (LUAD) and lung squamous carcinoma (LUSC) (Fig. 1a). Supporting this finding, an independent analysis of LUAD cohort GSE32867[31] demonstrated that *UHRF1* mRNA levels are upregulated in tumors, when compared with adjacent nonmalignant tissues (Fig. 1b). Moreover, analysis of an online dataset comprising 17 independent cohorts with 1411 total number of patients[32] revealed that high *UHRF1* expression correlates with reduced survival rates in lung cancer patients (Fig. 1c). Notably, analysis of mass spectrometry data from the Gillett et al. cohort[33] demonstrated increased UHRF1 protein expression in non-small cell lung cancer (NSCLC) tumor tissues (Fig. 1d). In addition, result of the Xu et al. cohort[34] suggested that higher levels of UHRF1 protein expression are correlated with poor NSCLC patient prognosis (Fig. 1e), which is consistent with a previous report[35]. Together, these findings indicate that high expression of UHRF1 correlates with the progression of NSCLC and poor prognosis of those patients.

To further investigate a possible functional role for UHRF1 in tumor development, we took advantage of CRISPR/Cas9 gene-editing technology to knockout *Uhrf1* in LG1233 cells, a murine lung adenocarcinoma cell line containing K-ras mutation and p53-loss derived from C57BL/6 mice[36] (Supplementary Fig. 1a). Following complete UHRF1 depletion, tumor growth was severely compromised: 1×10^5 LG1233 cells failed to establish tumors in immune-competent C57BL/6 mice; when inoculating 10-fold more tumor cells, UHRF1 inactivation still exhibited a 90% inhibition rate of tumor growth and longer survival of the animals (Fig. 1f–i). Similar levels of tumor suppression were observed in LG1233 tumors expressing the ovalbumin (OVA) antigen (Supplementary Fig. 1b, c). Partial loss of UHRF1 was also sufficient to retard tumor growth in vivo, as revealed by CRISPR interference (CRISPRi) technology[37,38]; moreover, tumor growth could be restored by reintroducing *Uhrf1* expression (Supplementary Fig. 1d, e).

To assess the generalizability of these findings, we genetically silenced *Uhrf1* in Lewis lung cancer cells (LLC) expressing the OVA antigen (Supplementary Fig. 1f). As with LG1233 cells, when transplanting LLC-OVA cells into immune-competent C57BL/6 mice, UHRF1 deficiency significantly slowed tumor growth compared with controls (Fig. 1j, l). Interestingly, UHRF1 inactivation produced only a mild decrease in tumor cell proliferation in culture (Supplementary Fig. 1g), consistent with previous reports that UHRF1 either promotes[39–41] or has a negligible impact on cell proliferation[42,43]. The growth difference between in vitro and in vivo indicates that the host immune system might be involved in UHRF1 inactivation-induced tumor suppression. In supporting this notion, we found that UHRF1 deficiency did not impact tumor growth in immune-compromised athymic nude mice (Fig. 1k, m), which lack mature T cells[44], demonstrating the critical role of adaptive immunity in the anti-tumor effect of UHRF1 inactivation. To evaluate the broader role of UHRF1 inactivation in tumor suppression, we also silenced *Uhrf1* in mouse MC38 colon cancer cells and B16 melanoma cells (Supplementary Fig. 1h, j). The absence of UHRF1 markedly inhibited the growth of both colon cancer and melanoma cells in syngeneic mouse hosts (Supplementary Fig. 1i, k). Taken together, these data demonstrate a general role for UHRF1 in promoting tumor growth across multiple cancer types, which is dependent on the evasion of the adaptive immune system by the tumor cells.

UHRF1 restrains CD8+ T cell response in the TME via down-regulation of MHC-I expression

To investigate UHRF1's role in immune evasion by tumor cells, we assessed the status of major immune components within the TME. Importantly, flow cytometric analysis revealed increased CD8+ T and NK cells in UHRF1-deficient LLC-OVA tumors (Fig. 2a). We also detected a significant intratumoral enrichment of CD8+ T cells in *Uhrf1*-knockout (Fig. 2b) or *Uhrf1*-knockdown (Supplementary Fig. 2a) LG1233 tumors. These results suggest that CD8+ T cells may be critical for tumor control in both tumor models. To test this possibility, we performed a CD8+ T cell depletion assay in tumor-bearing immune-competent mice. Indeed, CD8+ T cell ablation completely or partially restored the growth of UHRF1-deficient tumors (Fig. 2c, d, Supplementary Fig. 2b, c), consistent with the negligible effect of UHRF1 deficiency on tumor growth in athymic nude mice (Fig. 1k, m), pointing to a critical role for CD8+ T cells in restricting UHRF1-deficient tumor growth.

To further assess the impact of UHRF1 deficiency in tumor cells on CD8+ T cells, we assessed the cytokine production capacity of tumor-infiltrating CD8+ T cells. More IFNγ- and granzyme B

https://doi.org/10.1038/s41467-024-52902-5

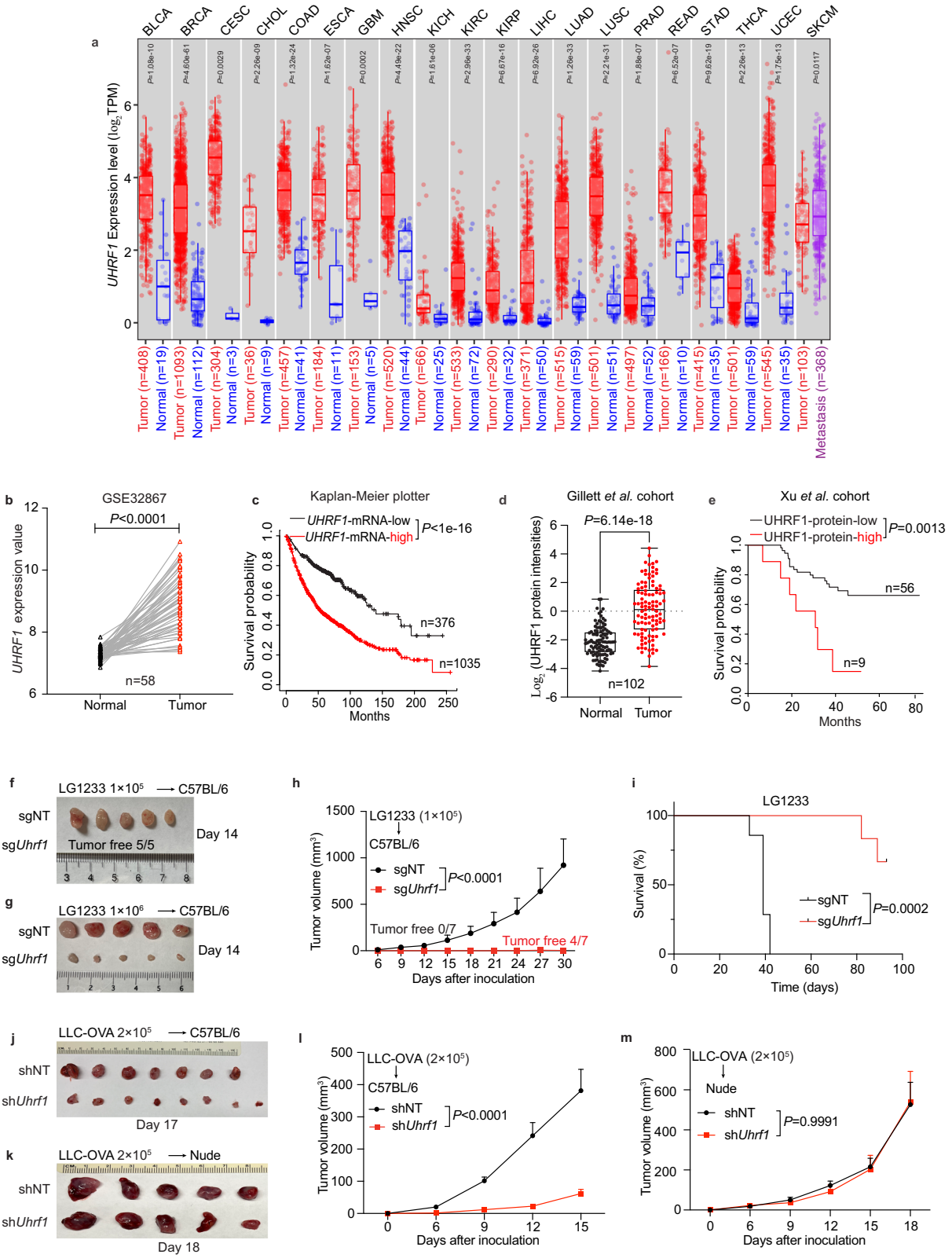

(GzmB)-producing CD8+ T cells were observed in UHRF1-deficient tumors (Fig. 2e). Moreover, there were more proliferating CD8+ T cells after UHRF1 deprivation (Fig. 2e). Next, we co-cultured OT-I T cells, which recognize the OVA antigen[45], with non-targeting control or UHRF1-deficient LG1233-OVA tumor cells (Supplementary Fig. 2d). Following the co-culture period, OT-I T cells in the UHRF1-deficient group were more readily activated, as indicated by elevated surface levels of CD69 (Fig. 2f), a well-known T cell activation marker[46,47]. Meanwhile, the OT-I T cells in UHRF1-deficient group secreted more effector molecules such as IFNγ, TNFα, and GzmB (Fig. 2g). In line with this, UHRF1-deficient tumor cells were more readily to be killed by OT-I cells (Supplementary Fig. 2e). Together, these data suggest enhanced T-cell activation in the absent of UHRF1.

Fig. 1 | UHRF1 is overexpressed in cancer and promotes tumor growth in syngenic mouse models. a UHRF1 expression in cancers versus normal tissues. TPM, transcripts per million. BLCA, bladder urothelial carcinoma; BRCA, breast invasive carcinoma; CESC, cervical squamous cell carcinoma; CHOL, cholangiocarcinoma; COAD, colon adenocarcinoma; ESCA, esophageal carcinoma; GBM, glioblastoma multiforme; HNSC, head and neck squamous cell carcinoma; KICH, kidney chromophobe; KIRC, kidney renal clear cell carcinoma; KIRP, kidney renal papillary cell carcinoma; LIHC, liver hepatocellular carcinoma; LUAD, lung adenocarcinoma; LUSC, lung squamous cell carcinoma; PRAD, prostate adenocarcinoma; READ, rectum adenocarcinoma; STAD, stomach adenocarcinoma; THCA, thyroid carcinoma; UCEC, uterine corpus endometrial carcinoma; SKCM, skin cutaneous melanoma. **b** UHRF1 expression in GSE32867 dataset ($n = 58$). **c** Survival analysis of lung cancer patients stratified by UHRF1 mRNA expression ($n = 376$ low, 1035 high). **d** UHRF1 Protein expression in Gillett et al. cohort ($n = 102$). **e** Survival analysis based on UHRF1 protein expression in Xu et al. cohort ($n = 56$ low, 9 high). **f**, **g** Tumor photos for LG1233 with 1×10^5 (**f**) or 1×10^6 (**g**) cells injected into female C57BL/6 mice. **h**, **i** Tumor growth (**h**) and survival(**i**) curves for LG1233 cells injected into female C57BL/6 mice. $n = 7$ per group. **j**, **l** Tumor photo (**j**) and growth curves (**l**) for LLC-OVA cells injected into female C57BL/6 mice. $n = 7$ (shNT), 8 (sh*Uhrf1*). **k**, **m** Tumor photo (**k**) and growth curves (**m**) for LLC-OVA cells injected into male nude mice. $n = 5$ per group. Data are mean ± SEM (**h, l, m**). For box plots, the box limits show the 25th to 75th percentile, the centre line shows the median value and the whiskers show the minimum to maximum values. *n* indicates the number of biological replicates. *P* values were determined using two-sided Wilcoxon signed-rank test (**a**, **b**, **d**), log-rank test (**c**, **e**, **i**), two-way ANOVA test (**h**, **l**, **m**). Source data are provided as a Source Data file. Data in (**h**, **i**, **l**, **m**) were repeated independently at least twice with similar results.

To unbiasedly assess the signaling pathways affected by UHRF1, we performed RNA-sequencing on WT and UHRF1-deficient bulk tumor tissues. Interestingly, among the upregulated genes in UHRF1-deficient tumors, the top-ranked pathways were T cell receptor binding, peptide antigen binding, and MHC-I protein binding (Fig. 2h). Given that impaired tumor antigen processing and presentation is a principal mechanism by which tumors evade immune recognition and elimination by CD8+ cytotoxic T cells[48], we hypothesized that UHRF1 may modulate MHC-I expression, consequently affecting T cell activation. Indeed, we noticed an increased expression of *H2k1* in RNA-seq data (Supplementary Fig. 2f). We further performed flow cytometry to measure the level of MHC-I molecules on tumor cell surface. The results showed that H2Kb-H2Db and HLA-ABC are significantly increased in UHRF1-deficient mouse and human tumor cells compared with non-targeting (NT) control cells (Fig. 2i, j, Supplementary Fig. 2g, h). Consequently, when the OVA peptide was loaded onto LG1233 tumor cells, UHRF1-deficient LG1233 tumor cells presented more OVA peptide on the tumor cell surface (Fig. 2k, Supplementary Fig. 2i). Furthermore, in the presence of IFNγ, which is known to enhance cell surface MHC-I expression in the TME[49], UHRF1-deficient tumor cells exhibited greater levels of OVA antigen presented on cell surface (Fig. 2k). To evaluate the role of UHRF1 on the antigen presentation of endogenous self-antigen, we expressed full-length OVA protein in LG1233 cells and detected SIINFEKL epitope presentation. As expected, more SIINFEKL epitope was presented on the UHRF1-deficient tumor cell surface (Supplementary Fig. 2j), indicating enhanced antigen processing and presentation following UHRF1 elimination. These data collectively suggest that UHRF1 may induce immune escape of tumor cells from recognition by CD8+ T cells, potentially through downregulation of MHC-I. Additionally, we also observed an enhanced type I interferon response, and increased endogenous retroviruses (ERV) gene expression (Supplementary Fig. 2k), both of which can induce innate immune response[50,51].

Cytoplasmic UHRF1 mediates MHC-I degradation in tumor cells within the TME

To systematically identify proteins interacting with MHC-I, which is widely presented on all nucleated cells[52], we transfected HEK293T cells with Flag-*HLAA*, followed by affinity purification of HLAA-containing protein complexes using anti-Flag antibody and subsequent mass spectrometry analysis. Interestingly, UHRF1 was among the top interacting proteins (Fig. 3a). To confirm this finding, we co-transfected Flag-*Uhrf1* and HA-*H2k1* plasmids into HEK293T cells. Co-immunoprecipitation (Co-IP) assays revealed that UHRF1 interacts with H2K1 (Fig. 3b). In addition to its role as an epigenetic regulator, UHRF1 is also recognized as an E3 ligase capable of ubiquitinating and degrading nuclear substrates, with several reports substantiating this biochemical function[42,53–55]. Given that proteolytic degradation is a well-known mechanism for restraining MHC-I expression[56–58], we reasoned that UHRF1 may bind to and ubiquitinate MHC-I, leading to its subsequent degradation. To test this postulation, we expressed HA-*H2k1* in both UHRF1-sufficient and -deficient tumor cells. Subsequent Co-IP assays revealed that ubiquitination levels of H2K1 were significantly reduced in UHRF1-deficient cells (Fig. 3c), suggesting that UHRF1 possesses the biochemical capability to facilitate MHC-I ubiquitination and degradation.

However, UHRF1 has been defined to function primarily in the nucleus, and the known substrates of its E3 ligase are nuclear proteins[42,53–55]. To address this intriguing question, we closely examined the expression pattern of UHRF1 protein in tumor tissue sections derived from NSCLC patients. We were surprised to find that 70% of tumor samples exhibit cytoplasmic UHRF1 staining in cancer cells in contrast to normal cells in the adjacent regions (Fig. 3d, e). To validate this highly unusual observation, we stained tissue samples from another lung cancer cohort using an independent UHRF1 antibody from a different vendor. Consistently, we observed more than 70% of patient samples from this cohort with cytoplasmic UHRF1 localization (Supplementary Fig. 3a, b). These results indicate that tumor cells not only highly express UHRF1 but also exhibit aberrant cytoplasmic localization detected in tissue samples derived from NSCLC patients. To probe this question further, we conducted immunofluorescence analysis in cultured LG1233 cells and found that UHRF1 was primarily located in the nucleus of the tumor cells; in contrast, UHRF1 was detected predominantly in the cytoplasm of LG1233 tumor tissues isolated from mice (Fig. 3f), consistent with IHC results from human cancer samples. Meanwhile, UHRF1 was consistently found in the nuclei of normal cells in mouse tissues (Fig. 3f). These observations suggest that cytoplasmic localization of UHRF1 occurs only in tumor cells grown in the TME, where UHRF1 could interact with MHC-I and cause its degradation.

Phosphorylation of UHRF1 regulates its cytoplasmic localization in response to factors in the TME, such as TGF-β

Previous studies found that phosphorylation of UHRF1 could be linked to its sequestration in the cytoplasm[59,60]. To test whether the TME-induced cytoplasmic translocation of UHRF1 is regulated by phosphorylation, we generated an antibody specifically recognizing phosphorylated UHRF1 on a specific serine residue (Ser661 in human and Ser656 in mouse; hereafter termed pUHRF1), based on findings from a zebrafish study[60]. We confirmed the specificity of this pUHRF1 antibody using HEK293T cells overexpressing Flag-tagged wild-type (WT) UHRF1 or Flag-tagged S661A mutant UHRF1, which is non-phosphorylable at this residue[60]. Western blot analysis showed that, whereas anti-UHRF1 antibody recognized both WT UHRF1 and the S661A mutant, the anti-pUHRF1 antibody exclusively recognized WT UHRF1 (Supplementary Fig. 4a). Immunofluorescent imaging analysis with the anti-pUHRF1 antibody further revealed a robust signal in the cytoplasm of tumor samples, in contrast with weak staining in normal lung tissues (Fig. 4a). Consistently, when we overexpressed Flag-*UHRF1* (S661A, resistant to phosphorylation) and Flag-*UHRF1* (S661D,

https://doi.org/10.1038/s41467-024-52902-5

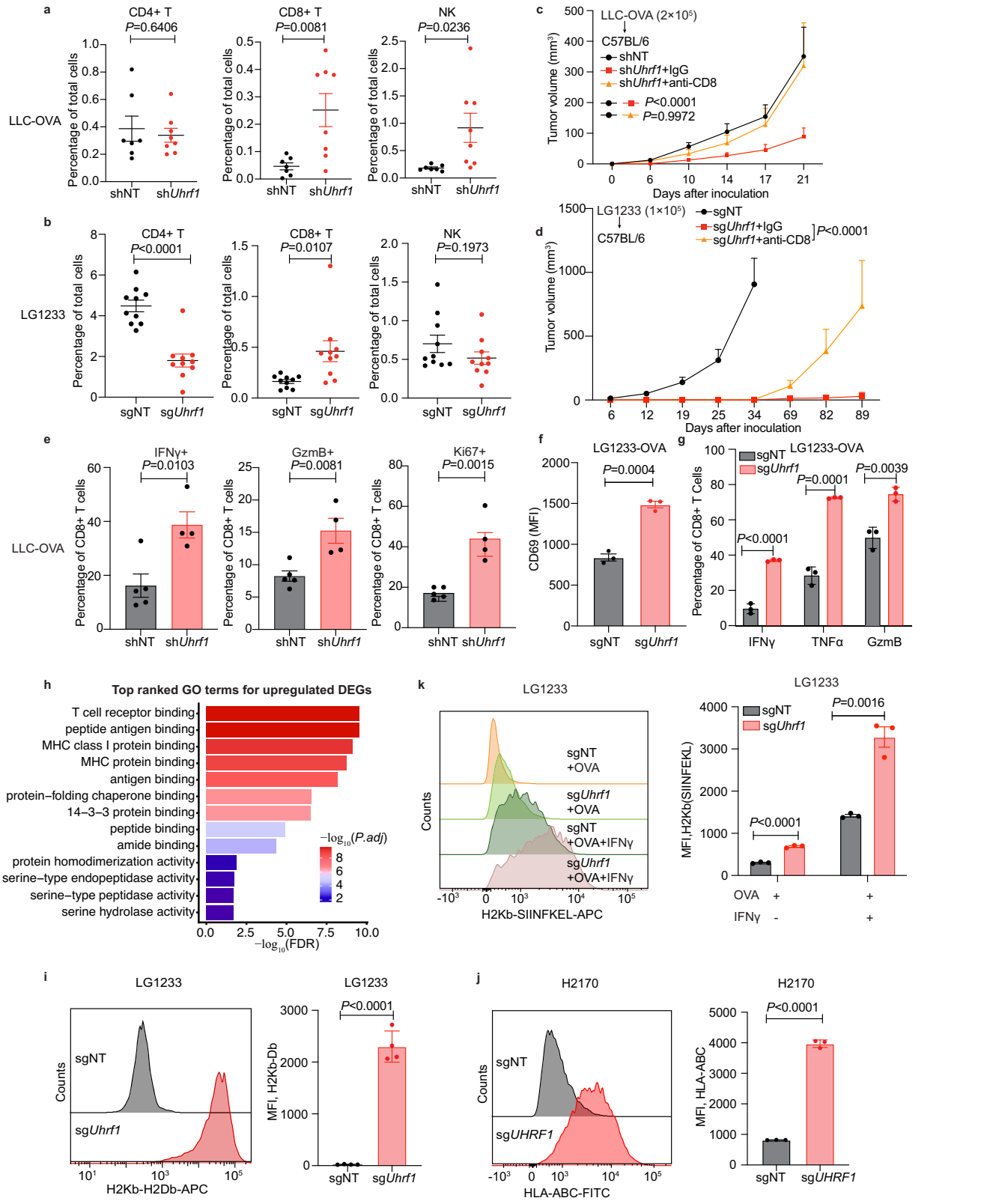

mimicking phosphorylation) into A549 human lung cancer cells, significantly higher cytoplasmic Flag signal was detected in Flag-*UHRF1* (S661D) overexpressing cells, while Flag-*UHRF1* (S661A) was mainly located in the nuclei (Supplementary Fig. 4b). These findings are consistent with previous reports showing that UHRF1 phosphorylated at Ser661 (mouse Ser656) is enriched in the cytoplasm[59,60]. Since we found that UHRF1 physically interacts with the MHC-I molecule (Fig. 3a, b), we next tested whether this interaction is regulated by UHRF1 phosphorylation. To investigate this, we co-transfected HA-*HLAA* with either wild-type, S661A, or S661D Flag-*UHRF1* and performed Co-IP analysis. This revealed that the phosphomimic S661D mutation significantly enhances the interaction between UHRF1 and MHC-I (Fig. 4b). Furthermore, immunofluorescence staining showed the co-localization of phosphorylated UHRF1 and MHC-I (Fig. 4c).

https://doi.org/10.1038/s41467-024-52902-5

Fig. 2 | UHRF1 restrains CD8+ T cell response through downregulate MHC-I expression. a, **b** Flow cytometry analysis of tumor-infiltrating lymphocytes. shNT or sh*Uhrf1* LLC-OVA cells were injected into female C57BL/6 mice, tumors were collected on day 17 for analysis, $n = 7$ (shNT), 8 (sh*Uhrf1*) (**a**); sgNT or sg*Uhrf1* LG1233 cells were injected into female C57BL/6 mice, tumors were collected on day 8 for analysis, $n = 10$ per group (**b**). **c**, **d** Tumor growth curves of tumor bearing female C57BL/6 mice treated with IgG or anti-CD8 neutralizing antibodies. $n = 6$ (shNT), 7 (sh*Uhrf1* + IgG, sh*Uhrf1*+anti-CD8)(**c**), $n = 7$ per group (**d**). **e** Flow cytometry assessing IFNγ+, GzmB+ and Ki67+ CD8+ T cells in shNT or sh*Uhrf1* tumors. $n = 5$ (shNT), 4 (sh*Uhrf1*). **f**, **g** Flow cytometry assessing CD69 expression (**f**) and cytokine production (**g**) in OT-I T cells co-cultured with sgNT or sg*Uhrf1* LG1233-OVA cells. $n = 3$ per group. **h** Gene set enrichment analysis (GO molecular function) of upregulated genes in sg*Uhrf1* tumors compared with sgNT tumors. $n = 3$ per group. **i** Flow cytometry determines the surface level of H2Kb-H2Db in LG1233 sgNT and sg*Uhrf1* cells. $n = 4$ per group. **j** Flow cytometry determines the surface level of HLA-ABC in sgNT and sg*UHRF1* H2170 cells. $n = 3$ per group. **k** Flow cytometry measurement of cell surface OVA 257-264 (SIINFEKL) peptide bound to MHC-I complex in LG1233 sgNT and sg*Uhrf1* cells, with or without 5 ng/mL IFNγ for 16 h. $n = 3$ per group. Data are mean ± SEM (**a**–**g**, **i**–**k**). *n* indicates the number of biological (**a**–**e**, **h**) or technical (**f**, **g** and **i**–**k**) replicates. *P* values were determined using two-tailed Student's *t* test (**a**, **b**, **e**–**g**, **i**–**k**), two-way ANOVA test (**c**, **d**) and one sided hypergeometric test then adjusted using multiple-test correction (**h**). MFI, mean fluorescence intensity; FDR, false discovery rate. Source data are provided as a Source Data file. All the data except **h** was repeated independently at least twice with similar results.

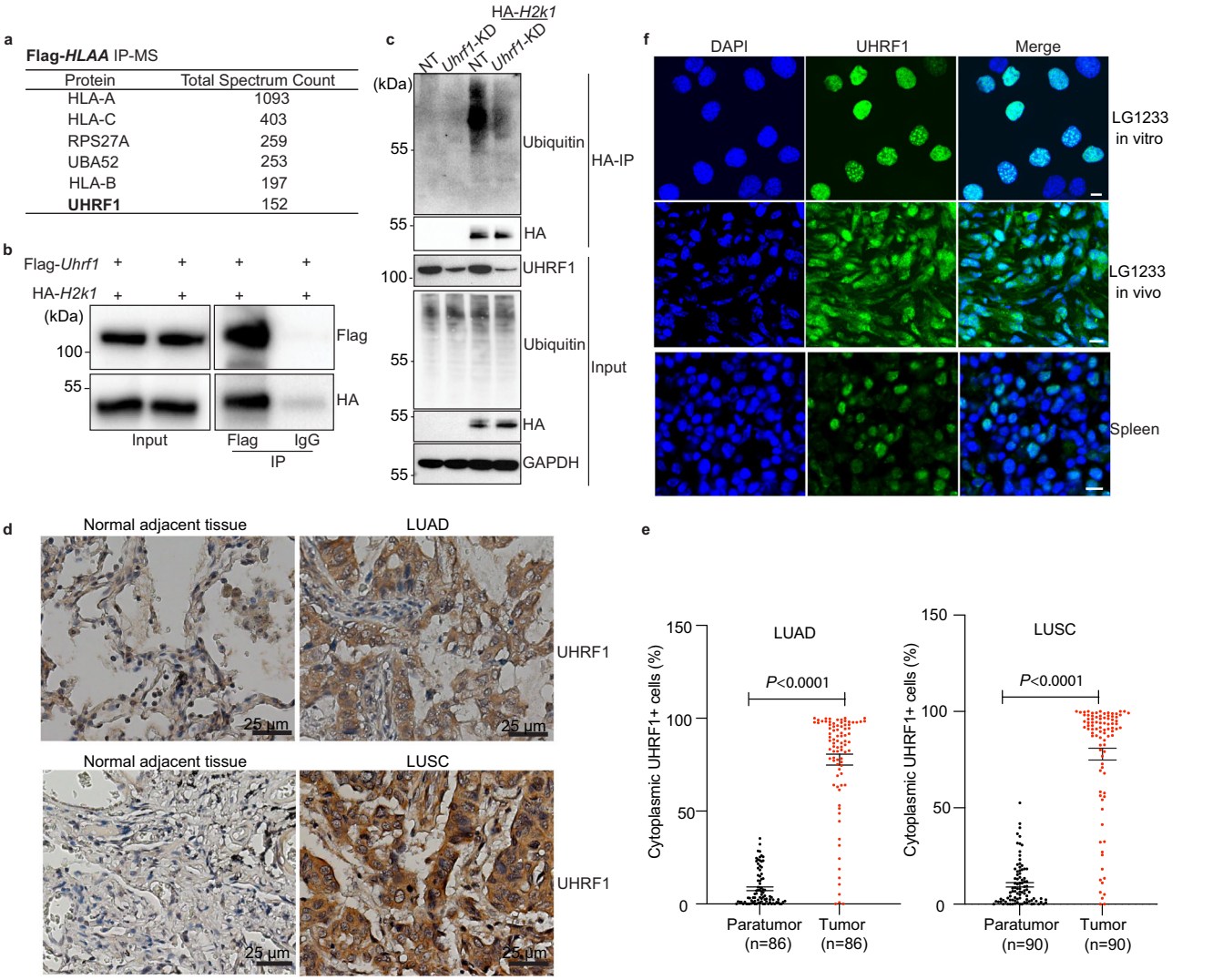

Fig. 3 | Cytoplasmic UHRF1 mediates MHC-I degradation. a Affinity purification of Flag-HLAA using antibody against Flag-tag. The top hits from mass spectrometry analysis were shown. **b** Interaction of mouse UHRF1 and H2K1 was determined by Co-immunoprecipitation (Co-IP). HEK293T cells were transfected with Flag-*Uhrf1* in combination with HA-*H2k1*. **c** Wild-type and *Uhrf1*-knockdown LLC-OVA cells were transfected with HA-*H2k1*. Ubiquitination of H2K1 was examined by Co-IP. **d** Representative images of UHRF1 expression by IHC staining from LUSC and LUAD patient samples and corresponding adjacent normal tissues. UHRF1 monoclonal antibody (H-8) from Santa Cruz (Cat# sc-373750) was used for the IHC staining. Scale bars, 25 μm. **e** Quantification of the cytoplasmic UHRF1 positive cells by Qupath from LUSC ($n = 90$) and LUAD ($n = 86$) patients with corresponding adjacent normal tissues. **f** Representative confocal images showing UHRF1 localization in cultured LG1233 cells (upper panel), LG1233 tumor tissues developed in C57BL/6 mice (middle panel) and normal spleen tissues (lower panel). Nuclei were stained with DAPI. Scale bars, 10 μm. *n* indicates the number of biological replicates. Data are mean ± SEM (**e**). *P* values were determined using two-tailed Student's *t* test (**e**). Data in (**b**, **c**, **f**) were repeated independently at least twice with similar results. Source data are provided as a Source Data file.

https://doi.org/10.1038/s41467-024-52902-5

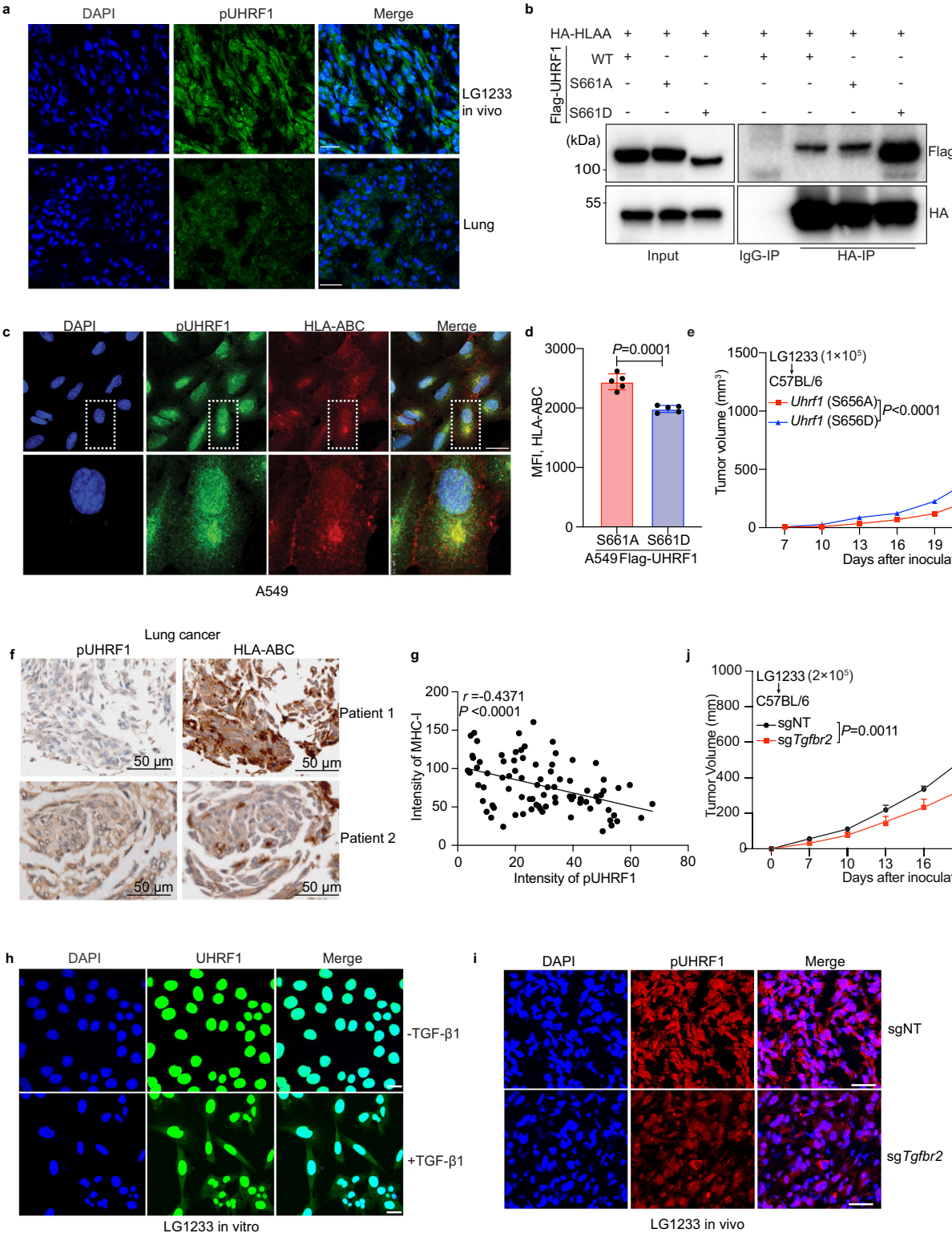

Moreover, MHC-I levels on the surface of Flag-*UHRF1* (S661D) overexpressing cells are reduced as compared with Flag-*UHRF1* (S661A) overexpressing cells (Fig. 4d). These data suggest that UHRF1 phosphorylation promotes its interaction with MHC-I to facilitate MHC-I degradation. Functionally, we found that overexpression of *Uhrf1* (S656D) in mouse LG1233 tumor cells notably enhanced tumor growth in immune-competent host, compared with the phosphorylation-resistant form *Uhrf1* (S656A) (Fig. 4e, Supplementary Fig 4c), likely through more effective suppression of MHC-I expression on cell surface. To evaluate the expression profile of pUHRF1 in human lung cancer, we stained patient samples with the antibody against pUHRF1 (S661). The expression pattern of pUHRF1 (S661) was similar among patients with stage I, II and III lung cancer and colon cancer, suggesting that the pUHRF1-mediated immune evasion may be involved in both early tumor development and advanced progression (Supplementary Fig. 4f). We next explored the relationship between pUHRF1 and MHC-I in patient samples. A negative correlation between pUHRF1 and HLA-ABC expression was observed in both lung cancer and colon cancer

Fig. 4 | Phosphorylated UHRF1 is localized to the cytoplasm in response to TGF-β within the TME. a Representative confocal images showing pUHRF1 (green) in LG1233 tumor tissues and normal lung tissues. Scale bars, 25 μm. **b** The UHRF1-HLAA interaction was examined by Co-IP. HEK293T cells were co-transfected with HA-HLAA and Flag-UHRF1 (wild-type, S661A or S661D). **c** Localization of HLA-ABC with pUHRF1. Dashed box regions were magnified. Scale bar, 25 μm. **d** Surface level of HLA-ABC in A549 cells with overexpressed Flag-UHRF1 (S661A) or Flag-UHRF1 (S661D), $n = 5$ per group. **e** LG1233 cells with S656A or S656D *Uhrf1* expression were subcutaneously injected into male C57BL/6 mice. Tumor volume was monitored. *Uhrf1* (S656A), $n = 7$; *Uhrf1* (S656D), $n = 8$. **f** Representative IHC images of pUHRF1 and HLA-ABC staining, showing low pUHRF1 with high HLA-ABC (patient 1) and high pUHRF1 with low HLA-ABC (patient 2). Scale bars, 50 μm. **g** Pearson correlation of pUHRF1 expression with HLA-ABC level in lung cancer samples ($n = 90$). **h** Representative confocal images showing LG1233 cells treated with or without 200 ng/mL TGF-β1 for 72 h, stained for UHRF1 (green) and DAPI (blue). Scale bars, 25 μm. **i** Representative confocal images showing pUHRF1 (red) localization in sgNT and sg*Tgfbr2* LG1233 tumor tissues. Scale bars, 25 μm. **j** Tumor growth curves of sgNT or sg*Tgfbr2* LG1233 cells injected into male C57BL/6 mice. $n = 6$ per group. Data are mean ± SD (**d**) and mean ± SEM (**e**, **j**). *n* indicates the number of biological (**e**, **j**) or technical (**d**) replicates. For (**g**), $n = 18$ of biological samples, five technical replicates in per biological sample were included. *P* values were determined using two-tailed Student's *t* test (**d**) and two-way ANOVA test (**e**, **j**), the correlation coefficient (*r*) and *P* value in (**g**) were determined using two-tailed Pearson correlation analysis. Data in (**a**–**d**, **h**, **i**) were repeated independently twice with similar results. MFI, mean fluorescence intensity. Source data are provided as a Source Data file.

patient samples (Fig. 4f, g, Supplementary Fig. 4d, e). Together, these results indicate that phosphorylated UHRF1 localized in the cytoplasm of tumor cells within the TME suppresses MHC-I to impair antigen presentation and curtail anti-tumor immunity.

The observation that UHRF1 cytoplasmic translocation happens only when tumor cells are grown in vivo strongly indicate that factors in the TME are responsible to stimulate its phosphorylation and translocation. In this regard, a previous report indicated that UHRF1 is sequestered outside the nucleus upon TGF-β stimulation during Treg differentiation[59]. Given the significant role of TGF-β in the TME across various solid tumor types[61,62], we postulated that TGF-β may facilitate UHRF1's nuclear-to-cytoplasmic translocation. To evaluate this, we treated LG1233 cells with recombinant mouse TGF-β protein for 72 h, and found a subset of tumor cells to display UHRF1 localization in the cytoplasm (Fig. 4h), which was accompanied by an increased UHRF1 phosphorylation (Supplementary Fig. 4g). To further confirm TGF-β's role in regulating UHRF1 cytoplasmic translocation, we employed the CRISPR-Cas9 technology to delete *Tgfbr2* in LG1233 cells (Supplementary Fig. 4h)[63]. Upon subcutaneous injection into mice, the loss of TGF-β signaling in tumor cells markedly reduced the amount of phosphorylated UHRF1 in the cytoplasm (Fig. 4i). Furthermore, *Tgfbr2*-KO in LG1233 tumor cells notably inhibited tumor growth in syngeneic mice compared with NT control cells (Fig. 4j). Collectively, these results suggest that TGF-β present in the TME could be one of the factors to induce cytoplasmic translocation of UHRF1, likely by initiating its phosphorylation. The phosphorylated UHRF1 then interacts with and facilitates the degradation of MHC-I, thereby promoting immune evasion and tumor growth. It is possible that other factors present within the TME could also contribute to the aberrant UHRF1 localization, either individually or in concert with TGF-β.

Inactivating UHRF1 induces memory formation via expansion of T cell clones with low-affinity TCRs and synergizes with anti-CTLA4-based ICB therapy

In our earlier study of the LG1233-OVA tumor model, UHRF1 deprivation eradicated a majority of tumors, while 100% mice died of NT control tumor progression (Supplementary Fig. 1b, c). Importantly, when these tumor-free mice were rechallenged with parental LG1233-OVA cells, 40% of them remained free of tumor initiation; in contrast, all naive mice died of tumor progression (Fig. 5a, b). This suggests that UHRF1 deprivation alone elicits a robust anti-tumor memory response, likely attributable to T cells with low-affinity TCRs[22,23]. To determine whether those T cells were induced by UHRF1 deprivation, we analyzed TCR affinity against OVA alternative peptide ligands[64], using the affinity index that we generated recently (Supplementary Fig. 5a)[23]. In *Uhrf1*-KO tumors, while the number of high-affinity OVA antigen-specific T cell clonotypes remained unchanged, we observed a significant increase in low-affinity OVA antigen-specific T cell clonotypes (Fig. 5c). To probe this further at the mechanistic level, we employed an approach to block the cytoplasmic translocation of UHRF1 by treatment of tumor-bearing mice with anti-TGF-β antibody. To start, OT-I T cells were primed with SIINFEKL (N4) or its weak avidity antigen variant peptide SIIQFEKL (Q4) from ovalbumin (OVA); their effector populations were then transferred into LG1233-OVA(N4) or (Q4) tumor-bearing mice presenting the corresponding peptide (Fig. 5d). Interestingly, high-affinity T cell-mediated therapy effectively slowed down tumor growth irrespective of anti-TGF-β treatment (Fig. 5e); however, treatment with anti-TGF-β antibody significantly increased the anti-tumor efficacy of low affinity T cells (Fig. 5f). Since inactivation of UHRF1 leads to increased expression of MHC-I on tumor cell surface, these data suggest that levels of MHC-I may determine the engagement of different spectrum of T cells with varying levels of TCR affinities, resulting with the expansion of low-affinity T cell pool critical for the formation of memory T cells in the presence of high levels of MHC-I.

Because tumor-intrinsic UHRF1 downregulates MHC-I to establish an immune cold TME, which is associated with resistance to ICB treatment[6], we next investigated whether UHRF1 inactivation may synergize with ICB therapy. Although genetic inactivation of UHRF1 did not enhance the anti-tumor efficacy of PD-1 blockade (Supplementary Fig. 5b), it did synergize with anti-CTLA4 treatment to significantly prolong the survival of tumor-bearing mice (Fig. 5g), so that 50% of mice in the combinational therapy group maintained long-term tumor control (Fig. 5h). Consistent with results on the LG1233-OVA tumor model shown earlier, all tumor-free survivors were resistant to rechallenge with parental tumor cells (Fig. 5i, Supplementary Fig. 5c), suggesting that a robust anti-tumor immune memory response was induced by the combined UHRF1 inactivation and anti-CTLA4 treatment.

To further elucidate the mechanistic nature of this combinational strategy, we characterized the intratumoral TCR repertoire, which can be shaped by ICB-based therapy[65]. Bulk tumor TCRβ-sequencing revealed that anti-CTLA4 monotherapy only mildly alters the TCR repertoire in NT LLC-OVA tumors (Fig. 5j), while significantly diminishing TCR similarity in *Uhrf1*-deficient tumors (Fig. 5k). Notably, UHRF1 inactivation alone results in a robust reduction in TCR similarity (Fig. 5l), which was even more pronounced when combined with anti-CTLA4 (Fig. 5m). Although the diversity of the entire intratumoral TCR pool was largely unaffected (Supplementary Fig. 5d–g), the size distribution of the TCR repertoire underwent significant changes. Specifically, while the top 10 most expanded T cell clonotypes comprised 16% of the entire repertoire in the control TME, in the *Uhrf1*-deficient TME with anti-CTLA treatment, this population increased to 25% of the entire repertoire (Fig. 5n). This suggests that the combinational therapy selectively expanded oligoclonal T cell populations within the TME. Collectively, these findings indicate that UHRF1 deficiency reshapes the intratumoral TCR repertoire landscape of tumor-infiltrating T cells and enhances the formation of memory T cells when combined with anti-CTLA4 treatment.

https://doi.org/10.1038/s41467-024-52902-5

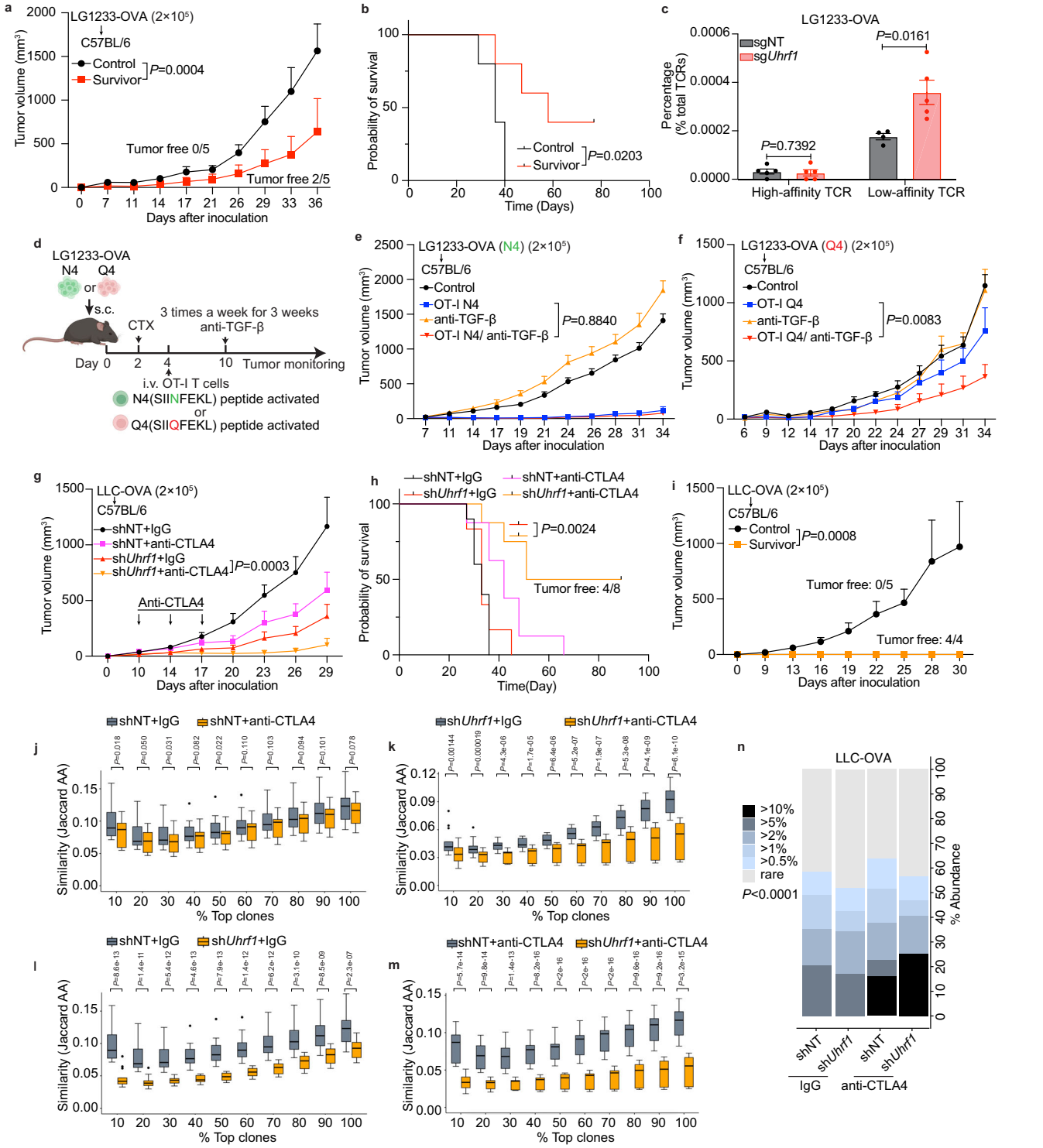

Fig. 5 | Inactivating UHRF1 induces memory formation via expansion of T cell clones with low-affinity TCRs and synergizes with anti-CTLA4-based ICB therapy. a, **b** Survivor mice that rejected *Uhrf1*-knockout tumors were rechallenged parental LG1233-OVA cells. Tumor growth (**a**) and survival (**b**) curves were plotted. $n = 5$ each group. **c** Frequency of high- and low-affinity TCR clonotypes in tumors from mice injected with sgNT or sg*Uhrf1* LG1233-OVA cells. $n = 5$ per group. **d** Schematic representation of T cell therapy. **e**, **f** Tumor growth curves of LG1233-OVA (N4) (**e**) or LG1233-OVA (Q4) (**f**) cells injected into male C57BL/6 mice. $n = 5$ per group. **g**, **h** Tumor growth (**g**) and survival (**h**) curves of female mice with shNT or sh*Uhrf1* tumors treated with anti-CTLA4 on days 7, 10 and 14. $n = 6$ per group (**g**). $n = 10$ (shNT+IgG), 8 (shNT+anti-CTLA4), 6 (sh*Uhrf1* + IgG), 8 (sh*Uhrf1*+anti-CTLA4) (**h**). **g**, **h** were performed independently. **i** Rechallenge of survivor mice from (**h**) with parental LLC-OVA cells. $n = 5$ (control), 4 (survivor). **j**–**n** TCRβ sequencing for LLC-OVA tumors. TCR similarity (**j**–**m**) and expanded TCR clones, constituting >10%, >5%, >2%, >1%, and >0.5% are shown as gradient segments (**n**). $n = 6$ (shNT +IgG, shNT+anti-CTLA4 and sh*Uhrf1* + IgG), 5 (sh*Uhrf1*+anti-CTLA4). Data are mean ± SEM (**a**, **c**, **e**–**g**, **i**). Box plots (**j**–**m**), the horizontal lines indicate the first, second (median) and third quartiles; the whiskers extend to ±1.5× the interquartile range. *n* indicates the number of biological replicates. *P* values were determined using two-way ANOVA test (**a**, **e**–**g**, **i**), log-rank test (**b**, **h**), two-tailed Student's *t* test (**c**, **j**–**m**) and Chi-square test (**n**). AA, amino acid. Source data are provided as a Source Data file.

Discussion

UHRF1, also known as Inverted CCAAT box Binding Protein of 90 kDa (ICBP90) in humans or nuclear protein of 95 kDa (Np95) in mice, has been extensively studied as a nuclear protein regulating DNA methylation and histone modifications[26]. By maintaining genomic integrity, UHRF1 actively participates in various physiological processes including spermatogenesis[66], embryonic development[67], interdigital tissue regression[68],and tissue repair and regeneration[39,69]. Under pathogenic conditions, compelling evidence suggests a strong link between UHRF1 overactivity and tumorigenesis in multiple cancers[35,70–72].Although extensively studied in malignancy, UHRF1 has been mainly defined as an epigenetic regulator to repress target genes, such as the tumor suppressors *RASSF1, CYGB and CDH13* in human lung adenocarcinoma cells[73]. In rare instances, UHRF1 has been detected in the cytoplasm, during Treg cell differentiation[59] and zebrafish development[60]. In this study, we unexpectedly found that UHRF1 exhibits aberrant cytoplasmic localization in tumor cells grown in vivo, as detected in both human patient samples and mouse tumor xenograft models, indicating that it acquired chromatin-independent activities conferring growth advantage for tumor cells within the TME, primarily through conferring an immune cold feature via downregulation of MHC-I. In the meantime, we do not discount its classic role as an epigenetic regulator in this context since UHRF1's PHD and SRA domains are important for maintaining DNA methylation levels[27], which has been demonstrated to affect tumor development. Structurally, it has been shown that an intramolecular interaction of UHRF1 is important for its histone association: the complex formation between the N-terminal tandem Tudor domain (TTD) and the C-terminal polybasic region (PBR) blocks UHRF1 binding to H3K9me3[74]. Since the mutation at human S661 (mouse S656) is located in the PBR domain, it is possible that the S661 mutant may disrupt UHRF1's ability to bind to histone, which needs further exploration.

In searching for factors in the TME that could induce the cytoplasmic translocation of UHRF1 via phosphorylation, we found that TGF-β, a known immune regulator[75], acts as one of such factors. It is possible that other factors in the TME could trigger the phosphorylation event, which is on a serine residue within a consensus sequence for CDK kinases, leading to the cytoplasmic translocation of this nuclear protein for the benefit of evading immune surveillance by tumor cells in the TME. The regulation of MHC-I, crucial for tumor immunity, has become a focal point of research in recent years[56–58,76,77]. Our findings indicate that cytoplasmic UHRF1 is involved in promoting the degradation of MHC-I molecules through ubiquitination at the post-translational level, which is consistent with its known function as an E3 ligase[42,54,78]. Considering the critical role of MHC-I and CD8+ T cells in the anti-cancer immunity process[79,80], these data suggest an additional role for UHRF1 in tumor immune surveillance, a notion supported by a recent study in which UHRF1 was identified as one of the top negative regulators of MHC-I through a targeted peptide-MHC I-guided CRISPR screen[56].

Given that nuclear UHRF1 plays a pivotal role in normal cell physiology[39], cytoplasmic phosphorylated UHRF1 might provide a rational target for cancer therapeutic drug development in the future to avoid systemic adverse effects. Here, we demonstrated the feasibility of this approach with genetic UHRF1 inactivation. Targeting UHRF1 combined with anti-CTLA4 ICB therapy significantly slows tumor growth and extends the survival of tumor-bearing mice. Moreover, this combinational therapy induces a strong anti-tumor memory response with long-term control over malignancy. Beyond switching an immune cold TME into a T cell-inflamed one, our TCRβ-seq data show that UHRF1 deficiency in combination with anti-CTLA4 therapy expands intratumoral oligoclonal T cell populations, indicating there are very limited numbers of tumor antigens. From this perspective, comparing with the negated additive effect of anti-PD-1 ICB, facilitating the antigen priming by CTLA4 blockade may represent a more effective way to enhance anti-tumor immune response. Known ICB resistance mechanisms include a lack of antigenic mutations, loss of tumor antigen expression, loss of HLA expression, alterations in antigen processing machinery, and constitutive PD-L1 expression[4]. In this regard, high levels of tumor-cell intrinsic UHRF1 may be used as a biomarker to predict ICB insensitivity, with targeting UHRF1 as a potential strategy to combat resistance to ICB therapy.

Based on our findings, UHRF1 inhibition could enhance anti-tumor immunity by increasing MHC-I presentation. In T cells, TGF-β signaling also induces UHRF1 phosphorylation and sequesters UHRF1 in the cytoplasm; as a result, DNA methylation of Foxp3 locus is decreased and induced regulatory T cells (iTreg) are generated[59]. From this perspective, blocking UHRF1 cytoplasmic localization or its upstream TGF-β signaling may also suppress iTreg cells development, which could alleviate immune suppression. Currently, UHRF1 inhibitors targeting DNA methylation (e.g., NSC232003)[81] are not yet clinically used. Since nuclear UHRF1 is very important for normal cell activities, it is not a suitable strategy to use inhibitors that can affect functions of nuclear UHRF1. Based on our results, targeting cytoplasmic UHRF1 in the future may offer a more specific and safer approach to combat cancer. In order to achieve a tumor specific UHRF1 inhibition, strategies may be considered to include 1) targeting TGF-β signaling to alter UHRF1 localization, as revealed by our study and others' work[59]; 2) preventing UHRF1 phosphorylation through CDK2 or CDK9 inhibition[42,59,60,82]; 3) potentially developing peptide-based inhibitors to disrupt UHRF1-MHC-I interactions.

High-affinity antigen-directed treatments, including CAR-T and TCR-T cell therapies, have had some success against both liquid and solid tumors[83,84]. However, these therapeutics can have considerable side effects, including cytokine release syndrome[85]. Low-affinity T cells are more readily to form memory in the contexts of infection and cancer[22,23], and induced by UHRF1 inactivation in tumor cells to elicit anti-tumor immunity. In the context of T cell-based therapies, targeting low-affinity antigens by evoking endogenous T cells has stimulated interest in TAAs as therapeutic targets[86]. From a translational point of view, evoking endogenous T cells by targeting UHRF1 would be highly desirable since depletion of tumor-intrinsic UHRF1 increases MHC-I expression and converts the tumor microenvironment from an immune cold into an immune hot state (Supplementary Fig. 6), representing a promising approach to improve the efficacy of immunotherapy.

Methods

Animals

All the animal experiments were approved by the Duke University Institutional Animal Care and Use Committee. Foxn1-null nude (athymic nude) mice (Strain: 007850) and C57BL/6 mice (Strain: 000664) were purchased from Jackson Laboratory. Thy1.1 + OT-I TCR transgenic mice were bred in house. Mice were housed under conditions at 22 °C, with a humidity between 30 and 70%, and a light cycle of 12h-12h on-off set.

Cell culture

A549, H2170, B16 and HEK293T cell lines were acquired from Duke University Cell Culture Facility, with original sourcing from ATCC. LLC-OVA cells were generated as previously described[87]. LG1233 cells were provided by T.Jacks (Massachusetts Institute of Technology). MC38 cells were purchased from Kerafast. Mycoplasma contamination was tested by Universal Mycoplasma Detection Kit (ATCC, 30-1012 K). A549, B16, MC38, HEK293T, LLC-OVA and LG1233 cells were cultured in Dulbecco's modified Eagle's medium (DMEM) supplemented with 10% fetal bovine serum and 100 U/mL penicillin-streptomycin. H2170 cells were cultured in RPMI-1640 medium supplemented with 10% fetal bovine serum and 100 U/mL penicillin-streptomycin. All cells were cultured at 37 °C in a humidified atmosphere with 5% CO_2.

Stable cell lines

HEK293T cells with approximately 70% confluency were transfected with vectors together with lentiviral packaging vectors PAX2 and VSV-G using Lipofectamine 2000 (Thermo Fisher Scientific, 11668019). Viral particles were collected and filtered after transfection for 48 h. For infection, lentiviral supernatant was added to cultured cells with 8 μg/mL Polybrene (Sigma-Aldrich, TR-1003). After incubation for 24 h, infected cells were selected for 3 to 5 days with 2 μg/mL puromycin (Thermo Fisher Scientific, A1113803). To generate *Uhrf1* knockdown cell line, shRNA targeting *Uhrf1* was purchased from Sigma-Aldrich. (Mouse-sh*Uhrf1*, 5′- CTGTAGCTCCAGTGCCGTTAA-3′). To generate knockout cell lines, sgRNAs were designed based on webtool (https://chopchop.cbu.uib.no/)[88] and cloned according to Dr. Feng Zhang laboratory's protocol[89,90]. The sequences of sgRNAs used in this study are:

mouse-sg*Uhrf1*: 5′-CATCATAATCGAAGAGTGTG-3′,
human-sg*UHRF1*: 5′-CGGGGCTTCTGGTACGACG-3′,
mouse-sg*Tgfbr2*: 5′-ACCTGCAGGAGTACCTCACG-3′

To generate stable LG1233 cell line with OVA expression, wild-type OVA (N4) and its Q4 mutant were cloned into *pWPT* (Addgene, #12255), LG1233-OVA(N4)-T2A-GFP cells and LG1233-OVA(Q4)-T2A-Scarlet cells were sorted by FACS for 2 rounds with purity more than 95%.

Tumor models

In the mouse tumor experiments, 2×10^5 LLC-OVA; 1×10^5, 2×10^5 or 1×10^6 LG1233 (-OVA); 1×10^6 MC38 and 2×10^5 B16 cells were subcutaneously injected into C57BL/6 mice (6 to 8 weeks old). 2×10^5 LLC-OVA cells were subcutaneously injected into athymic nude mice (6 to 8 weeks old). The specific gender of the mice, along with the number of cells injected for each experiment, are detailed in the corresponding figure legends. Both male and female mice were used in animal studies. Tumor volumes were calculated using the following formula: $0.52 \times a \times b^2$, where a is the larger diameter and b is the smaller diameter of the tumor mass. The permitted maximal tumor size was 2000 mm^3 by Duke University Institutional Animal Use and Care Committee. Mice were euthanized once tumor size reached 2000 mm^3. In some instances, malignant tumors exhibited explosive growth, potentially exceeding 2000 mm^3. Mice with oversized tumors were euthanized with CO_2 immediately upon discovery.

In vivo lymphocyte depletion and ICB therapy

Depletion of lymphocytes in C57BL/6 mice was conducted by injection of neutralizing antibodies. In brief, mice were given intraperitoneal injection of antibodies against CD8 (100 μg, twice a week, Bio X Cell, BE0223) or recommended isotype control (Bio X Cell, BE0088). All deletion assays were initiated one day before tumor cell inoculation. Specific cell deletion was confirmed by flow cytometry at experimental endpoints. For ICB therapy treatments, tumor-bearing mice were intraperitoneally injected with 200 μg anti-mouse PD-1 antibodies (Bio X Cell, BE0033-2) or IgG isotype control (Bio X Cell, BE0290); and 30 μg anti-mouse CTLA-4 antibodies (Bio X Cell, BP0164) or IgG isotype control (Bio X Cell, BP0086) on the indicated days.

Molecular cloning

The coding sequences for mouse *Uhrf1* and human *UHRF1* were purchased from Horizon. Mutant variants of human UHRF1 (S661A, S661D) were generated by PCR. The coding sequence for *HLAA* was cloned from Addgene plasmid (#85162)[91]. The coding sequence for *H2k1* was cloned from cDNA of mouse embryonic fibroblast (MEF) cells. These coding sequences were subsequently cloned into pSIN-lentiviral vectors using the Gibson Assembly (New England Biolabs). Details of the primers used are listed in Supplementary Table 1.

Adoptive T cell transfer

For the adoptive transfer of OT-I T cells, lymph nodes and spleens from OT-I TCR transgenic mice were mechanically dissociated. Red blood cells were lysed using ACK lysing buffer (Quality Biological). After isolation, OT-I T cells were activated in vitro for 48 h with 1 μg/mL OVA N4 or Q4 peptide, then cultured with 50 U/mL hIL-2 (Peprotech, 200-02). 2×10^5 LG1233-OVA (N4 or Q4) tumor cells were subcutaneously injected into male C57BL/6 mice. On day 2, each tumor-bearing mouse received 2 mg cyclophosphamide (Sigma-Aldrich, C7397) for lymphodepletion before T cell transfer. On day 4, mice were intravenously injected with 1×10^6 OT-I T cells per mouse. 10 days after inoculation, mice were treated with isotype control antibody (10 mg/kg, Bio X cell, BE0083) or anti-TGF-β (10 mg/kg, Bio X Cell, BE0057) as previously described[92]. Briefly, antibodies were administered 3 times a week for 3 weeks. The first dose was delivered intravenously, and subsequent doses were given intraperitoneally.

Western blots

Total protein was extracted and lysed in RIPA buffer (Thermo Fisher Scientific) with 1% protease and phosphatase inhibitor cocktail (Thermo Fisher Scientific), and protein concentrations were determined using the BCA protein assay kit (Thermo Fisher Scientific). Equal amounts of protein in the lysates were boiled in SDS loading buffer. Protein samples were loaded and fractionated on a 4–12% SDS-PAGE gel and then transferred to a polyvinylidene difluoride membrane, which was subsequently blocked in 5% skim milk in Tris-buffered saline with 0.1% Tween-20 (TBST buffer). Primary antibodies against total proteins or phosphorylated forms of protein were applied, followed by secondary antibodies (Thermo Fisher Scientific) incubation and visualized using an enhanced chemiluminescent horseradish peroxidase substrate (Thermo Fisher Scientific). A protein ladder (Thermo Fisher Scientific) was used to determine molecular mass in the western blot analysis. The western blot primary antibodies, their source and dilution information as follows. Anti-UHRF1(Santa Cruz Biotechnology, sc-373750, 1:1000); Anti-Flag (Sigma, F1804, 1:5000); Anti-HA (Sigma, H3663, 1:2000); Anti-TGFBR2 (Santa Cruz Biotechnology, sc-17791, 1:500), Anti-β-Actin (Proteintech, 66009-1-Ig, 1: 5000), anti-Ubiquitin (Cell Signaling Technology, 43124, 1:1000), GAPDH (Santa Cruz Biotechnology, sc-365062, 1:5000). The polyclonal antibody recognizing human phosphorylated Ser-661(mouse Ser-656) in UHRF1 was generated by LifeTein, LLC, as previously reported[60]. The antigen used was a synthetic phosphoserine peptide corresponding to residues 654-659 of human UHRF1, denoted as CGPSRAG(pS)PRRTSKKT-KLH.

Immunoprecipitation

Cells were transfected with the indicated constructs for 24 h, washed briefly, and then lysed on ice using lysis buffer (Cell Signaling Technology, 9806) for 1 h. Lysates containing 1 mg of total protein were precleared with magnetic Protein G Dynabeads (Thermo Fisher, 10003D) and incubated overnight at 4 °C with either 2 μg of the indicated antibodies or with an isotype control. The immunoprecipitates were collected with magnets, and the pellets were washed with lysis buffer and stored in 2× sample buffer prior to western blot analysis. Mass spectrometry analysis was conducted at the Proteomics and Metabolomics Core Facility at Duke University. IP samples were analyzed by LC-MS using an Orbitrap Fusion Lumos mass spectrometer. Database searches were performed against the SwissProt Homo sapiens database. A total of 2 samples were analyzed, including one IgG control and one Flag-HLAA pull down sample.

Flow cytometry

For in vitro experiments, cultured cancer cells were resuspended and stained with APC anti-mouse H-2Kb/H-2Db (28-8-6) (Biolegend, 114614, 1:100), FITC anti-human HLA-ABC (W6/32) (Biolegend, 311404, 1:100) and APC anti-mouse H-2Kb bound to SIINFEKL (25-D1.16) (Biolegend, 141605, 1:100) at 4 °C for 30 min in the dark. After washing with PBS, the surface expression of MHC-I or the MHC-I bound endogenous OVA peptide was analyzed on an BD FACS Canto flow cytometer using BD

FACS DIVA SOFTWARE (Duke University Flow Cytometry Shared Facility), and data were analyzed using FlowJo. To analyze tumor-infiltrating lymphocytes, murine tumor tissues were mechanically dissociated and digested with 1 mg/mL collegenase type I (GIBCO, 17100-017) by incubating at 37 °C for 60 min. The cells were filtered with a 70 μm cell strainer. Red blood cells were removed with ACK lysis buffer. Single cell suspensions were stained with NearIR-LIVE/DEAD fixable dead cell dye (Invitrogen, 1:2000), followed by incubation with the following cell surface antibodies for 30 min at 4 °C in the dark. After washing with PBS, cells were then subjected to flow cytometry analysis as described above. The following antibodies were used to identify immune cell populations in TME: FITC anti-mouse CD45 (30-F11) (Biolegend, 103108, 1:100), PE anti-mouse TCR vβ8.3 (1B3.3) (BioLegend, 156304, 1:100), PE/Cyanine7 anti-mouse CD4 (RM4-5) (Biolegend, 100528, 1:100), PerCP/Cyanine5.5 anti-mouse CD8β (YTS156.7.7) (Biolegend, 126610, 1:100), APC anti-mouse NK-1.1 (PK136) (Biolegend, 108710, 1:100), PE/Cyanine7 anti-mouse CD69 (H1.2F3) (BioLegend, Cat. 104511, 1:100). For intracellular staining, the Intracellular Fixation & Permeabilization Buffer Set (eBioscience™, 88-8824-00) was used to fix and permeabilize cells, followed by staining with Pacific Blue anti-mouse IFN-γ (XMG1.2) (Biolegend, 505818, 1:100), PE/Cyanine7 anti-human/mouse Granzyme B (QA16A02) (Biolegend, 372214, 1:100), APC anti-mouse TNFα (MP6-XT22) (BioLegend, 506308, 1:100), Pacific Blue anti-mouse Ki-67 (16A8) (BioLegend, 652421, 1:100). Flow cytometry gating strategies are shown in Supplementary Fig. 7.

Immunofluorescence

For immunofluorescence analysis, frozen tumor samples were sectioned into 8 μm slices. Cultured cells were seeded on a sterile glass coverslip and maintained in complete medium. LG1233 cells were treated with or without 200 ng/mL recombinant mouse TGF-β1 protein (R&D, 7666-MB-005/CF) for 72 h prior to IF staining. Briefly, tumor tissues or culture cells were fixed with 4% paraformaldehyde (PFA) for 15 min at room temperature. After fixation, samples were permeabilized using 0.1% Triton X-100 in PBS for 10 min and then blocked with 5% BSA for 1 h at room temperature. The cells or tissue sections were incubated with the primary antibodies against UHRF1 (Santa Cruz Biotechnology, sc-373750, 1:200), pUHRF1 (LifeTein, customized, 1:200), anti-HLA-ABC (Proteintech, Cat. 15240-1-AP, 1:200) and Flag (Sigma, F1804, 1:200) at 4 °C overnight. Subsequently, samples were incubated with fluorescently-labeled secondary antibodies for 1 h at room temperature. Tissues or cells were counterstained with DAPI. Finally, slides were mounted using ProLong Diamond antifade mountant (ThermoFisher, P36965) and images were captured with a Leica SP5 inverted confocal microscope.

Immunohistochemistry

Lung cancer tissue arrays in Fig. 3 were obtained from Shanghai Outdo Biotechnology Company Ltd. Lung cancer tissue arrays in Fig. 4 and colon cancer tissue arrays in Supplementary Fig 4 were purchased from TissueArray.com. Lung cancer tissue sections in Supplementary Fig 3 were obtained from West China Hospital, Chengdu, China, which was approved by the ethics committees of West China Hospital, Chengdu, China. Briefly, slides were heated until tissue transparency was achieved, followed by sequential xylene and ethanol washes, and a rinse in water. Antigen retrieval was performed using Rodent Decloaker buffer (Bio Care Medical) in a pressure cooker set to 95 °C for 20 min. Next, 3% hydrogen peroxide solution (VWR, BDH7690-1) was used to block endogenous peroxidases and subsequently washed with 0.1% TBS-T (Tween-20) wash buffer. Slides were then blocked with 5% BSA for 1 h at room temperature. Primary anti-UHRF1 (Santa Cruz Biotechnology, sc-373750, 1:100), anti-UHRF1 (Abnova, H00029128-M01, 1:100), anti-pUHRF1 (LifeTein, LLC, customized, 1:100) and anti-HLA-ABC (Proteintech, 15240-1-AP, 1:1000) antibodies were diluted accordingly in the blocking buffer and incubated overnight at 4 °C. Next day, secondary antibodies were used to incubate at room temperature for 1 h. After wash 4 times with TBST buffer, DAB chromogen (DAKO, K3468) was added to slides and monitoring for brown color development. After the desired staining intensity was achieved, slides were rinsed with distilled water. Hematoxylin was applied and slides were then treated with a bluing reagent, dehydrated, and mounted using Cytoseal (Thermo Scientific, 8312-4). The images were captured by using Zeiss Axio Imager Z2. QuPath was used for quantification, images were analyzed using the H-DAB staining option, with cytoplasmic DAB thresholds set at >0.3. A minimum of 100 cells per slide were analyzed.

T-cell activation assay

CD8+ T cells were isolated from lymph nodes of OT-I mice. OT-I T cells were co-cultured with sgNT or sg*Uhrf1* LG1233-OVA cells at a ratio of 1:1. 16 h after co-culture, T cells were stained with anti-CD69-PE/Cy7 (Biolegend,105512, H1.2F3, 1:100). For intracellular staining, T cells were fixed and permeabilized, followed by staining with Pacific Blue anti-mouse IFN-γ(XMG1.2) (Biolegend, 505818, 1:100), PE/Cyanine7 anti-human/mouse Granzyme B (QA16A02) (Biolegend, 372214, 1:100), APC anti-mouse TNFα (MP6-XT22) (BioLegend, 506308, 1:100). Cells were acquired by flow cytometry analysis.

LDH release assay

Cytotoxicity was assessed using the LDH release assay (Promega, G1780) according to the manufacturer's instructions. Briefly, LG1233-OVA target cells were seeded at a density of 6000 cells/well in a 96-well plate. OT-1 T cells were added at effector-to-target (E:T) ratio of 1:1 and the co-cultures were incubated for 8 h. Subsequently, the culture supernatants were carefully harvested to avoid disturbing the cell pellet. LDH release, indicative of target cell lysis, was quantified using the enzymatic assay provided in the kit. Cytotoxicity percentage was calculated using % Cytotoxicity = [(Experimental−Effector Spontaneous−Target Spontaneous)/(Target Maximum−Target Spontaneous)] × 100%, where Experimental represents LDH activity in wells with both effector and target cells, Effector Spontaneous is the background LDH release from effector cells alone, Target Spontaneous from target cells alone, and Target Maximum from target cells lysed with detergent to determine maximum LDH release. All assays were performed in quadruplicate to ensure reproducibility and statistical reliability.

Antigen presentation assay

sgNT and sg*Uhrf1* LG1233 cells were treated with 5 ng/mL recombinant murine IFNγ protein (Peprotech, 315-05) for 16 h. After treatment, the cells were collected and incubated with 1 μg/mL OVA(SIINFEKL) peptide in a 37 °C water bath for 1 h. Subsequently, the cells were washed twice with PBS and stained with APC-conjugated anti-mouse SIINFEKL bound H-2Kb (25-D1.16) (Biolegend, 141605, 1:100) at 4 °C for 1 h. After wash with PBS, the samples were proceeded for flow cytometry analysis.

RNA-seq

1×10^6 sgNT or sg*Uhrf1* LG1233-OVA cells were subcutaneously injected into female C57BL/6 mice. Tumor tissues were collected on day 27. Total RNA was extracted using ZYMO RESEARCH kit (Direct-zol RNA miniprep, cat. No. R2052) and dissolved in RNase-free water. Library construction and RNA sequencing were performed by Novogene. Briefly, mRNA was purified, and first strand cDNA was synthesized using random hexamer primers followed by the second stand cDNA synthesis. After end repair, A-tailing, adapter ligation, size selection, amplification, and purification, quantified libraries were pooled and sequenced on Illumina platform (NovaSeq PE150).

For RNA-seq data analysis, fastp v0.20.157 was used for read trimming and STAR v2.7.5a58 for mapping to the Gencode GRCm38 genome. Quality filtering was applied with Samtools v1.1859. Gene counts were derived using featureCounts v2.0.160 and analyzed with

DESeq2 v1.36.061, filtering for genes with >5 reads in >3 samples. *P* values were adjusted using the Benjamini-Hochberg method. Significant DEGs (adjusted $p < 0.05$) underwent hierarchical clustering with the R package pheatmap v1.0.12 and volcano plot visualization with EnhancedVolcano v1.14.0. GO enrichment was performed with R package clusterProfiler v4.4.462.

TCRβ sequencing

For LG1233-OVA tumor model, 1×10^6 LG1233-OVA sgNT or sg*Uhrf1* cancer cells were inoculated into female C57BL/6 mice. Tumors were collected on day 27. For LLC-OVA tumor model, 2×10^5 shNT or sh*Uhrf1* LLC-OVA cells were inoculated into male C57BL/6 mice and subsequently treated with either 30 μg IgG or CTLA4 antibodies on days 7, 10 and 14. Tumors were collected on day 17. Total RNA was extracted from the bulk tumor tissues for TCR library construction using the Direct-zol RNA MiniPrep kit (Zymo reseach, 11-331). In brief, 1 μg of purified RNA was converted into cDNA, followed by amplification of the CDR3 region of rearranged TCRB loci using a multiplex PCR system. A set of forward primers, each tailored for specific TCR Vβ segments, and a reverse primer for the TCRB constant region to produce amplicons spanning the entire CDR3 region. The PCR products were run on a 2.5% agarose gels, targeted bands were purified using QIAquick Gel Extraction kit, and then sent for sequencing at on an Illumina platform at Novogene (NovaSeq PE150). Primers for TCRβ sequencing are provided in Supplementary Table 1. For data analysis, raw sequencing data was preprocessed and aligned to TCR gene segments using MiXCR software[93]. A two-step assembly was applied to create an extensive profile of TCR clonotypes, focusing on the CDR3 region. Clonotypes were expanded, error-corrected, and quantified. Diversity and Similarity within TCR repertoires were measured using Shannon entropy and Jaccard indices, respectively, based on the analysis of amino acid sequences. The diversity and similarity analysis were conducted using R immunarch package.

Statistics and reproducibility

No statistical method was used to predetermine sample size. Experimental sample size was chosen based on commonly accepted standards. We excluded one outlier sample in Fig. 5c by performing Grubbs' test which calculated with GraphPad. Mice were randomly assigned to each group, other experiments were not randomized. The investigators were not blinded to allocation during experiments and outcome assessment. Statistical analysis was conducted using GraphPad Prism 8 software. *P* values less than 0.05 were considered statistically significant and are presented in the figures by the value. Two-way ANOVA was used for multiple comparison in tumor growth experiments. Log-rank tests were used for survival analyses. Two-tailed Student's *t*-tests or Wilcox tests were used to compare between two groups. The correlation coefficient (*r*) and *P* value were obtained from Pearson correlation analysis. Chi-square test was used for comparison of the different percentage of expanded clones in different groups.

Reporting summary

Further information on research design is available in the Nature Portfolio Reporting Summary linked to this article.

Data availability

RNA and TCRβ sequencing data have been deposited in the Gene Expression Omnibus (GEO) under accession number GSE272880 and GSE261146 respectively. The mass spectrometry proteomics data have been deposited to the ProteomeXchange Consortium via the PRIDE[94] partner repository with the dataset identifier PXD051193. The human tumor and adjacent data were generated from Tumor IMmune Estimation Resource (TIMER) (https://cistrome.shinyapps.io/timer/), source data from the TCGA Research Network (http://cancergenome.nih.gov/). The correlation data between UHRF1 expression and survival rate in lung cancer patients (Fig. 1c) was downloaded from http://kmplot.com website[32]. This study did not generate any unique code or algorithm. The algorithms used for all analysis in this study are public available. Source data are provided with this paper.

References

1. Ferris, R. L. et al. Nivolumab for recurrent squamous-cell carcinoma of the head and neck. *N. Engl. J. Med.* **375**, 1856–1867 (2016).
2. McDermott, D. F. et al. Atezolizumab, an anti-programmed death-ligand 1 antibody, in metastatic renal cell carcinoma: long-term safety, clinical activity, and immune correlates from a phase ia study. *J. Clin. Oncol.* **34**, 833–842 (2016).
3. Chen, D. S. & Mellman, I. Oncology meets immunology: the cancer-immunity cycle. *Immunity* **39**, 1–10 (2013).
4. Sharma, P., Hu-Lieskovan, S., Wargo, J. A. & Ribas, A. Primary, adaptive, and acquired resistance to cancer immunotherapy. *Cell* **168**, 707–723 (2017).
5. Bai, R. et al. Mechanisms of cancer resistance to immunotherapy. *Front. Oncol.* **10**, 1290 (2020).
6. Gettinger, S. et al. Impaired HLA Class I antigen processing and presentation as a mechanism of acquired resistance to immune checkpoint inhibitors in lung cancer. *Cancer Discov.* **7**, 1420–1435 (2017).
7. de Visser, K. E. & Joyce, J. A. The evolving tumor microenvironment: from cancer initiation to metastatic outgrowth. *Cancer Cell* **41**, 374–403 (2023).
8. Martinez-Reyes, I. & Chandel, N. S. Cancer metabolism: looking forward. *Nat. Rev. Cancer* **21**, 669–680 (2021).
9. Weis, S. M. & Cheresh, D. A. Tumor angiogenesis: molecular pathways and therapeutic targets. *Nat. Med.* **17**, 1359–1370 (2011).
10. Harris, A. L. Hypoxia-a key regulatory factor in tumour growth. *Nat. Rev. Cancer* **2**, 38–47 (2002).
11. Duan, Q., Zhang, H., Zheng, J. & Zhang, L. Turning cold into hot: firing up the tumor microenvironment. *Trends Cancer* **6**, 605–618 (2020).
12. Joyce, J. A. & Fearon, D. T. T cell exclusion, immune privilege, and the tumor microenvironment. *Science* **348**, 74–80 (2015).
13. Cai, L. et al. Defective HLA class I antigen processing machinery in cancer. *Cancer Immunol. Immunother.* **67**, 999–1009 (2018).
14. Dhatchinamoorthy, K., Colbert, J. D. & Rock, K. L. Cancer immune evasion through loss of MHC class I antigen presentation. *Front. Immunol.* **12**, 636568 (2021).
15. Fruh, K. & Yang, Y. Antigen presentation by MHC class I and its regulation by interferon gamma. *Curr. Opin. Immunol.* **11**, 76–81 (1999).
16. Grasso, C. S. et al. Conserved interferon-gamma signaling drives clinical response to immune checkpoint blockade therapy in melanoma. *Cancer Cell* **38**, 500–515.e503 (2020).
17. Gide, T. N. et al. Distinct immune cell populations define response to anti-PD-1 monotherapy and anti-PD-1/anti-CTLA-4 combined therapy. *Cancer Cell* **35**, 238–255.e236 (2019).
18. Dagogo-Jack, I. & Shaw, A. T. Tumour heterogeneity and resistance to cancer therapies. *Nat. Rev. Clin. Oncol.* **15**, 81–94 (2018).
19. Aleksic, M. et al. Different affinity windows for virus and cancer-specific T-cell receptors: implications for therapeutic strategies. *Eur. J. Immunol.* **42**, 3174–3179 (2012).
20. Stone, J. D., Harris, D. T. & Kranz, D. M. TCR affinity for p/MHC formed by tumor antigens that are self-proteins: impact on efficacy and toxicity. *Curr. Opin. Immunol.* **33**, 16–22 (2015).
21. Yu, W. et al. Clonal deletion prunes but does not eliminate self-specific alphabeta CD8(+) T lymphocytes. *Immunity* **42**, 929–941 (2015).
22. Knudson, K. M., Goplen, N. P., Cunningham, C. A., Daniels, M. A. & Teixeiro, E. Low-affinity T cells are programmed to maintain normal primary responses but are impaired in their recall to low-affinity ligands. *Cell Rep.* **4**, 554–565 (2013).

23. Yin, T. et al. Breaking NGF–TrkA immunosuppression in melanoma sensitizes immunotherapy for durable memory T cell protection. *Nat. Immunol.* **25**, 268–281 (2024).
24. Sharma, S., Kelly, T. K. & Jones, P. A. Epigenetics in cancer. *Carcinogenesis* **31**, 27–36 (2010).
25. Grolleau-Julius, A., Ray, D. & Yung, R. L. The role of epigenetics in aging and autoimmunity. *Clin. Rev. Allergy Immunol.* **39**, 42–50 (2010).
26. Nishiyama, A. et al. Uhrf1-dependent H3K23 ubiquitylation couples maintenance DNA methylation and replication. *Nature* **502**, 249–253 (2013).
27. Kong, X. et al. Defining UHRF1 domains that support maintenance of human colon cancer DNA methylation and oncogenic properties. *Cancer Cell* **35**, 633–648.e637 (2019).
28. Li, T. et al. TIMER2.0 for analysis of tumor-infiltrating immune cells. *Nucleic Acids Res.* **48**, W509–W514 (2020).
29. Li, T. et al. TIMER: a web server for comprehensive analysis of tumor-infiltrating immune cells. *Cancer Res.* **77**, e108–e110 (2017).
30. Li, B. et al. Comprehensive analyses of tumor immunity: implications for cancer immunotherapy. *Genome Biol.* **17**, 174 (2016).
31. Gao, J. et al. Integrative analysis of complex cancer genomics and clinical profiles using the cBioPortal. *Sci. Signal* **6**, pl1 (2013).
32. Gyorffy, B. Transcriptome-level discovery of survival-associated biomarkers and therapy targets in non-small-cell lung cancer. *Br. J. Pharmacol.* **181**, 362–374 (2023).
33. Gillette, M. A. et al. Proteogenomic characterization reveals therapeutic vulnerabilities in lung adenocarcinoma. *Cell* **182**, 200–225.e235 (2020).
34. Xu, J. Y. et al. Integrative proteomic characterization of human lung adenocarcinoma. *Cell* **182**, 245–261.e217 (2020).
35. Unoki, M. et al. UHRF1 is a novel diagnostic marker of lung cancer. *Br J Cancer* **103**, 217–222 (2010).
36. Dimitrova, N. et al. Stromal expression of miR-143/145 promotes neoangiogenesis in lung cancer development. *Cancer Discov.* **6**, 188–201 (2016).
37. Larson, M. H. et al. CRISPR interference (CRISPRi) for sequence-specific control of gene expression. *Nat. Protoc.* **8**, 2180–2196 (2013).
38. Alerasool, N., Segal, D., Lee, H. & Taipale, M. An efficient KRAB domain for CRISPRi applications in human cells. *Nat Methods* **17**, 1093–1096 (2020).
39. Xiang, H. et al. UHRF1 is required for basal stem cell proliferation in response to airway injury. *Cell Discov.* **3**, 17019 (2017).
40. Tien, A. L. et al. UHRF1 depletion causes a G2/M arrest, activation of DNA damage response and apoptosis. *Biochem. J.* **435**, 175–185 (2011).
41. Li, Q., Chu, Z. & Geng, S. UHRF1 knockdown attenuates cell growth, migration, and invasion in cutaneous squamous cell carcinoma. *Cancer Invest.* **39**, 84–97 (2021).
42. Zhang, H. et al. A cell cycle-dependent BRCA1-UHRF1 cascade regulates DNA double-strand break repair pathway choice. *Nat. Commun.* **7**, 10201 (2016).
43. Tian, Y. et al. UHRF1 contributes to DNA damage repair as a lesion recognition factor and nuclease scaffold. *Cell Rep.* **10**, 1957–1966 (2015).
44. Cordier, A. C. & Haumont, S. M. Development of thymus, parathyroids, and ultimo-branchial bodies in NMRI and nude mice. *Am. J. Anat.* **157**, 227–263 (1980).
45. Clarke, S. R. et al. Characterization of the ovalbumin-specific TCR transgenic line OT-I: MHC elements for positive and negative selection. *Immunol. Cell Biol.* **78**, 110–117 (2000).
46. Cibrian, D. & Sanchez-Madrid, F. CD69: from activation marker to metabolic gatekeeper. *Eur. J. Immunol.* **47**, 946–953 (2017).
47. Simms, P. E. & Ellis, T. M. Utility of flow cytometric detection of CD69 expression as a rapid method for determining poly- and oligoclonal lymphocyte activation. *Clin. Diagn. Lab Immunol.* **3**, 301–304 (1996).
48. Morrison, B. J., Steel, J. C. & Morris, J. C. Reduction of MHC-I expression limits T-lymphocyte-mediated killing of Cancer-initiating cells. *BMC Cancer* **18**, 469 (2018).
49. Zhou, F. Molecular mechanisms of IFN-gamma to up-regulate MHC class I antigen processing and presentation. *Int. Rev. Immunol.* **28**, 239–260 (2009).
50. Goel, S. et al. CDK4/6 inhibition triggers anti-tumour immunity. *Nature* **548**, 471–475 (2017).
51. Magnani, E. et al. uhrf1 and dnmt1 loss induces an immune response in zebrafish livers due to viral mimicry by transposable elements. *Front. Immunol.* **12**, 627926 (2021).
52. Lerner, E. C. et al. CD8(+) T cells maintain killing of MHC-I-negative tumor cells through the NKG2D-NKG2DL axis. *Nat. Cancer* **4**, 1258–1272 (2023).
53. Ubiquitin ligase activity of UHRF1. https://doi.org/10.1091/mbc.E05- (2005).
54. Ma, J. et al. Ubiquitin E3 ligase UHRF1 regulates p53 ubiquitination and p53-dependent cell apoptosis in clear cell renal cell carcinoma. *Biochem. Biophys. Res. Commun.* **464**, 147–153 (2015).
55. Foster, B. M. et al. Critical role of the UBL domain in stimulating the E3 ubiquitin ligase activity of UHRF1 toward chromatin. *Mol. Cell* **72**, 739–752.e739 (2018).
56. Chen, X. et al. A membrane-associated MHC-I inhibitory axis for cancer immune evasion. *Cell* **186**, 3903–3920.e21 (2023).
57. Liu, X. et al. Inhibition of PCSK9 potentiates immune checkpoint therapy for cancer. *Nature* **588**, 693–698 (2020).
58. Yamamoto, K. et al. Autophagy promotes immune evasion of pancreatic cancer by degrading MHC-I Supplementary. *Nature* **581**, 100–105 (2020).
59. Sun, X., Cui, Y., Feng, H., Liu, H. & Liu, X. TGF-beta signaling controls Foxp3 methylation and T reg cell differentiation by modulating Uhrf1 activity. *J Exp Med* **216**, 2819–2837 (2019).
60. Chu, J. et al. UHRF1 phosphorylation by cyclin A2/cyclin-dependent kinase 2 is required for zebrafish embryogenesis. *Mol. Biol. Cell* **23**, 59–70 (2012).
61. Pickup, M., Novitskiy, S. & Moses, H. L. The roles of TGFbeta in the tumour microenvironment. *Nat. Rev. Cancer* **13**, 788–799 (2013).
62. Derynck, R., Turley, S. J. & Akhurst, R. J. TGFbeta biology in cancer progression and immunotherapy. *Nat. Rev. Clin. Oncol.* **18**, 9–34 (2021).
63. Fix, S. M. et al. CRISPR-mediated TGFBR2 knockout renders human ovarian cancer tumor-infiltrating lymphocytes resistant to TGF-beta signaling. *J. Immunother. Cancer* **10**, e003750 (2022).
64. Zehn, D., Lee, S. Y. & Bevan, M. J. Complete but curtailed T-cell response to very low-affinity antigen. *Nature* **458**, 211–214 (2009).
65. Rudqvist, N. P. et al. Radiotherapy and CTLA-4 blockade shape the TCR repertoire of tumor-infiltrating T cells. *Cancer Immunol. Res.* **6**, 139–150 (2018).
66. Wu, Y. et al. UHRF1 establishes crosstalk between somatic and germ cells in male reproduction. *Cell Death Dis.* **13**, 377 (2022).
67. Sharif, J. et al. The SRA protein Np95 mediates epigenetic inheritance by recruiting Dnmt1 to methylated DNA. *Nature* **450**, 908–912 (2007).
68. Sanchez-Fernandez, C., Lorda-Diez, C. I., Garcia-Porrero, J. A., Montero, J. A. & Hurle, J. M. UHRF genes regulate programmed interdigital tissue regression and chondrogenesis in the embryonic limb. *Cell Death Dis.* **10**, 347 (2019).
69. Sakai, H. et al. Uhrf1 governs the proliferation and differentiation of muscle satellite cells. *iScience* **25**, 103928 (2022).
70. Mudbhary, R. et al. UHRF1 overexpression drives DNA hypomethylation and hepatocellular carcinoma. *Cancer Cell* **25**, 196–209 (2014).
71. Zhou, L. et al. Regulation of UHRF1 by miR-146a/b modulates gastric cancer invasion and metastasis. *FASEB J.* **27**, 4929–4939 (2013).

72. Wang, F. et al. UHRF1 promotes cell growth and metastasis through repression of p16(ink(4)a) in colorectal cancer. *Ann. Surg. Oncol.* **19**, 2753–2762 (2012).
73. Daskalos, A. et al. UHRF1-mediated tumor suppressor gene inactivation in nonsmall cell lung cancer. *Cancer* **117**, 1027–1037 (2011).
74. Gao, L. et al. An intramolecular interaction of UHRF1 reveals dual control for its histone association. *Structure* **26**, 304–311.e303 (2018).
75. Nixon, B. G., Gao, S., Wang, X. & Li, M. O. TGFbeta control of immune responses in cancer: a holistic immuno-oncology perspective. *Nat. Rev. Immunol.* **23**, 346–362 (2023).
76. Gu, S. S. et al. Therapeutically increasing MHC-I expression potentiates immune checkpoint blockade. *Cancer Discov.* **11**, 1524–1541 (2021).
77. Burr, M. L. et al. An evolutionarily conserved function of polycomb silences the MHC class I antigen presentation pathway and enables immune evasion in cancer. *Cancer Cell* **36**, 385–401.e388 (2019).
78. Du, Z. et al. DNMT1 stability is regulated by proteins coordinating deubiquitination and acetylation-driven ubiquitination. *Sci. Signal* **3**, ra80 (2010).
79. Mellman, I., Chen, D. S., Powles, T. & Turley, S. J. The cancer-immunity cycle: Indication, genotype, and immunotype. *Immunity* **56**, 2188–2205 (2023).
80. Giles, J. R., Globig, A. M., Kaech, S. M. & Wherry, E. J. CD8(+) T cells in the cancer-immunity cycle. *Immunity* **56**, 2231–2253 (2023).
81. Myrianthopoulos, V. et al. Tandem virtual screening targeting the SRA domain of UHRF1 identifies a novel chemical tool modulating DNA methylation. *Eur. J. Med. Chem.* **114**, 390–396 (2016).
82. Johnson, J. L. et al. An atlas of substrate specificities for the human serine/threonine kinome. *Nature* **613**, 759–766 (2023).
83. Hong, M., Clubb, J. D. & Chen, Y. Y. Engineering CAR-T cells for next-generation cancer therapy. *Cancer Cell* **38**, 473–488 (2020).
84. Shafer, P., Kelly, L. M. & Hoyos, V. Cancer therapy with TCR-engineered T cells: current strategies, challenges, and prospects. *Front. Immunol.* **13**, 835762 (2022).
85. Brudno, J. N. & Kochenderfer, J. N. Recent advances in CAR T-cell toxicity: mechanisms, manifestations and management. *Blood Rev.* **34**, 45–55 (2019).
86. Hollingsworth, R. E. & Jansen, K. Turning the corner on therapeutic cancer vaccines. *NPJ Vaccines* **4**, 7 (2019).
87. Hopewell, E. L. et al. Lung tumor NF-kappaB signaling promotes T cell-mediated immune surveillance. *J. Clin. Invest.* **123**, 2509–2522 (2013).
88. Labun, K. et al. CHOPCHOP v3: expanding the CRISPR web toolbox beyond genome editing. *Nucleic Acids Res.* **47**, W171–W174 (2019).
89. Shalem, O. et al. Genome-scale CRISPR-Cas9 knockout screening in human cells. *Science* **343**, 84–87 (2014).
90. Sanjana, N. E., Shalem, O. & Zhang, F. Improved vectors and genome-wide libraries for CRISPR screening. *Nat. Methods* **11**, 783–784 (2014).
91. Walchli, S. et al. Invariant chain as a vehicle to load antigenic peptides on human MHC class I for cytotoxic T-cell activation. *Eur. J. Immunol.* **44**, 774–784 (2014).
92. Mariathasan, S. et al. TGFbeta attenuates tumour response to PD-L1 blockade by contributing to exclusion of T cells. *Nature* **554**, 544–548 (2018).
93. Bolotin, D. A. et al. MiXCR: software for comprehensive adaptive immunity profiling. *Nat. Methods* **12**, 380–381 (2015).
94. Perez-Riverol, Y. et al. The PRIDE database resources in 2022: a hub for mass spectrometry-based proteomics evidences. *Nucleic Acids Res.* **50**, D543–D552 (2022).

Acknowledgements

The authors thank Dr. Guohong Li at Wuhan University for providing assistance during manuscript revision. We thank Dr. Yongsheng Wang at West China Hospital for help with IHC staining for human lung cancer tissues. We thank the staff of the Duke University Flow Cytometry Shared Resource, Duke Light Microscopy Core Facility, and the Proteomics and Metabolomics Core Facility for help with data acquisition. We thank Dr. Zhao Zhang from Duke University for assistance with drawing illustrations. Schematics in Fig.5d (*BioRender.com/u82q392*) and Supplementary Figs. 2d (*BioRender.com/e87x601*), 2i (*BioRender.com/k25b929*), 5a (*BioRender.com/o76j936*), 5c (*BioRender.com/j18n557*) and 6 (*BioRender.com/y71m947*) were created *in BioRender. Tan, L. (2024)* with modifications and released under a Creative Commons Attribution-NonCommercial-NoDerivs 4.0 International license. This work was supported by R01-CA233205 from the NIH to X.-F.W. and Q.-J.L. Q.-J.L. is supported by core research grants provided to the IMCB and SIgN by the BMRC, A*STAR and National Research Foundation (NRF) Singapore under the NRF Investigatorship (NRFI09-0016).

Author contributions

Conceptualization, L.T., T.Y., H.X., Q.-J.L., and X.-F.W.; experimental study, L.T., T.Y., H.X., J.C., Y.D., G.W., B.J.W.L., D.H., Y.L., K.X., C.Y., Z.M.; bioinformatics analysis, L.W., P.M., E.W., Y.H., M.T.; writing and editing, L.T., T.Y., P.B.A., Q.-J.L. and X.-F.W.; supervision, Q.-J.L. and X.-F.W.

Competing interests

Q.-J.L. is a scientific co-founder and shareholder of TCRCure Biopharma and Hervor Therapeutics. The other authors declare no competing interests.

Additional information

Supplementary information The online version contains supplementary material available at https://doi.org/10.1038/s41467-024-52902-5.

Correspondence and requests for materials should be addressed to Qi-Jing Li or Xiao-Fan Wang.

Peer review information *Nature Communications* thanks Iannis Aifantis, Cheng Cheng Zhang and the other, anonymous, reviewer(s) for their contribution to the peer review of this work. A peer review file is available.